

## The Magnetic Field of Mercury

**Brian J. Anderson · Mario H. Acuña · Haje Korth · James A. Slavin · Hideharu Uno · Catherine L. Johnson · Michael E. Purucker · Sean C. Solomon · Jim M. Raines · Thomas H. Zurbuchen · George Gloeckler · Ralph L. McNutt Jr.**

Received: 13 April 2009 / Accepted: 5 June 2009 / Published online: 9 July 2009  
© Springer Science+Business Media B.V. 2009

**Abstract** The magnetic field strength of Mercury at the planet's surface is approximately 1% that of Earth's surface field. This comparatively low field strength presents a number of challenges, both theoretically to understand how it is generated and observationally to distinguish the internal field from that due to the solar wind interaction. Conversely, the small field also means that Mercury offers an important opportunity to advance our understanding both of planetary magnetic field generation and magnetosphere-solar wind interactions. The observations from the Mariner 10 magnetometer in 1974 and 1975, and the MESSENGER Magnetometer and plasma instruments during the probe's first two flybys of Mercury on 14 January and 6 October 2008, provide the basis for our current knowledge of the internal field. The external field arising from the interaction of the magnetosphere with the solar wind is more prominent near Mercury than for any other magnetized planet in the Solar System, and particular attention is therefore paid to indications in the observations of deficiencies in

---

Mario H. Acuña deceased 5 March 2009.

B.J. Anderson (✉) · H. Korth · R.L. McNutt Jr.  
Applied Physics Laboratory, The Johns Hopkins University, Laurel, MD 20723, USA  
e-mail: [Brian.Anderson@jhuapl.edu](mailto:Brian.Anderson@jhuapl.edu)

M.H. Acuña · M.E. Purucker  
Solar System Exploration Division, NASA Goddard Space Flight Center, Greenbelt, MD 20771, USA

J.A. Slavin  
Heliophysics Science Division, NASA Goddard Space Flight Center, Greenbelt, MD 20771, USA

C.L. Johnson · H. Uno  
Department of Earth and Ocean Sciences, University of British Columbia, Vancouver, BC V6T 1Z4, Canada

S.C. Solomon  
Department of Terrestrial Magnetism, Carnegie Institution of Washington, Washington, DC 20015, USA

G. Gloeckler · J.M. Raines · T.H. Zurbuchen  
Department of Atmospheric, Oceanic and Space Sciences, University of Michigan, Ann Arbor, MI 48109, USA

our understanding of the external field. The second MESSENGER flyby occurred over the opposite hemisphere from the other flybys, and these newest data constrain the tilt of the planetary moment from the planet's spin axis to be less than  $5^\circ$ . Considered as a dipole field, the moment is in the range 240 to 270 nT $\cdot R_M^3$ , where  $R_M$  is Mercury's radius. Multipole solutions for the planetary field yield a smaller dipole term, 180 to 220 nT $\cdot R_M^3$ , and higher-order terms that together yield an equatorial surface field from 250 to 290 nT. From the spatial distribution of the fit residuals, the equatorial data are seen to reflect a weaker northward field and a strongly radial field, neither of which can be explained by a centered-dipole matched to the field measured near the pole by Mariner 10. This disparity is a major factor controlling the higher-order terms in the multipole solutions. The residuals are not largest close to the planet, and when considered in magnetospheric coordinates the residuals indicate the presence of a cross-tail current extending to within  $0.5R_M$  altitude on the nightside. A near-tail current with a density of  $0.1 \mu\text{A}/\text{m}^2$  could account for the low field intensities recorded near the equator. In addition, the MESSENGER flybys include the first plasma observations from Mercury and demonstrate that solar wind plasma is present at low altitudes, below 500 km. Although we can be confident in the dipole-only moment estimates, the data in hand remain subject to ambiguities for distinguishing internal from external contributions. The anticipated observations from orbit at Mercury, first from MESSENGER beginning in March 2011 and later from the dual-spacecraft BepiColombo mission, will be essential to elucidate the higher-order structure in the magnetic field of Mercury that will reveal the telltale signatures of the physics responsible for its generation.

**Keywords** Mercury · Magnetic field · Magnetosphere · MESSENGER · BepiColombo

## 1 Introduction

The presence or absence of a magnetic field on a terrestrial planet depends on the interplay of several interior processes. Mercury, the smallest of the inner planets, illustrates the challenges facing an understanding of the origins of planetary magnetism. If Mercury had a pure iron core, thermal history models predict that such a core would now be completely solid, and thus Mercury would have at most a remanent crustal magnetic field (e.g., Solomon 1976). The discovery by Mariner 10 that Mercury has a weak but Earth-like internal magnetic field (Ness et al. 1974, 1975) hinted that the planet's core contains sufficient lighter elements to lower the melting temperature and permit a presently fluid outer core (e.g., Schubert et al. 1988). Accounting for a weak, primarily dipolar field in terms of an Earth-like core dynamo has proved challenging, but a variety of numerical dynamo models have been explored that can predict such a field (Heimpel et al. 2005; Stanley et al. 2005; Christensen 2006; Takahashi and Matsushima 2006; Glassmeier et al. 2007a, 2007b). To test such ideas, considerable effort has gone into extracting as much information as possible about the geometry of the internal field from Mariner 10 observations (Ness 1979; Connerney and Ness 1988; Engle 1997).

The flybys of Mercury by NASA's MERcury Surface, Space ENvironment, GEOchemistry, and Ranging (MESSENGER) spacecraft (Solomon et al. 2001, 2007) on 14 January and 6 October 2008 have yielded new magnetic field observations (Anderson et al. 2007, 2008b; Slavin et al. 2008, 2009a, 2009b) and the first plasma ion observations within the planet's magnetosphere (Zurbuchen et al. 2008). As a result of those encounters, we are now in a position to reassess the nature of Mercury's internal magnetic field. Any such consideration necessarily involves a careful treatment of external field sources. The small internal field

at Mercury implies that external current systems are particularly important, because they produce magnetic fields at the surface that are comparable in strength to the planetary field (e.g., Slavin and Holzer 1979). This fact, together with the limited trajectories over which in situ observations are available from the Mariner 10 and MESSENGER flybys to date, leads to a situation in which the internal field is difficult to separate from the external and plasma pressure contributions to the magnetic field observations (Connerney and Ness 1988; Korth et al. 2004). In addition to considering what we can deduce about the internal magnetic field, we identify those aspects of the external field description that are most critical for the Mercury system and need to be further understood.

## 2 Processes Responsible for Magnetic Fields at Mercury

There are three candidate sources of magnetic fields arising within the planet: a core dynamo, crustal magnetization, and induction currents in any electrically conducting regions. The amplitude of Mercury's annual forced libration, recently detected by Earth-based radar observations (Margot et al. 2007), implies that the planet has a fluid outer core. The presence of a light element in an otherwise iron-rich core can permit a presently molten outer core; most specific models of such thermal histories for Mercury have been based on the proposition that sulfur is the principal light element (Schubert et al. 1988; Hauck et al. 2004), although other elements considered as candidate components of the Earth's outer core (e.g., Si, O, H, C) might yield a similar outcome. Early proposals for a remanent origin for Mercury's dipolar internal field (Stephenson 1976; Srnka 1976) were questioned on the grounds that a high specific magnetization would be required and the polarity of the field would have to be stable during the time the crust cooled through the Curie temperature of the relevant magnetic carriers (Schubert et al. 1988). The detection of strong crustal magnetic fields on Mars (Acuña et al. 1999) and the recognition that the thickness of a magnetized crustal layer on Mercury could vary with latitude and longitude (Aharonson et al. 2004) renewed consideration of crustal sources of Mercury's internal field. In addition to fields from these sources, the suite of external currents that must be considered include magnetopause, magnetotail, and perhaps other currents resulting from solar wind plasma interaction that are as yet poorly understood for Mercury. We discuss these processes in turn.

### 2.1 Internal Field Sources: Crustal, Dynamo, and Induced

The presence of at least a thin shell of molten material in the outer core raises the possibility that the planet supports a dynamo driven by thermal convection or chemical buoyancy (Stevenson 1983; Stanley et al. 2005; Heimpel et al. 2005). A variety of models for such a dynamo have been investigated (Heimpel et al. 2005; Christensen 2006; Stanley et al. 2007; Wicht et al. 2007; Christensen and Wicht 2008), and these models make generally distinct predictions for the long-wavelength structure of the planetary field. A thin-shell dynamo could yield significant non-dipolar structure in the field (e.g., Stanley et al. 2007), which although attenuated at spacecraft altitudes might be diagnostic of a minimum shell thickness. Thick-shell dynamos can also yield a weak field, and a stable but conductive layer at the top of the core could suppress higher-order terms, so such models are generally consistent with an axisymmetric dipolar field at spacecraft altitudes (Christensen 2006; Wicht et al. 2007; Christensen and Wicht 2008). Mineral physics experiments suggest that a stable layer at the top of Mercury's outer core is a plausible hypothesis (Chen et al. 2008).

It has also been proposed that the large-scale field could be due to a dynamo generated by thermoelectric currents along a rough core-mantle boundary (Stevenson 1987; Giampieri and Balogh 2002). Observational constraints on the multipolar structure and dipole axis orientation relative to the rotation axis may be important discriminators among these hypotheses.

Another physical mechanism that may account for the weak global-scale planetary field is crustal remanence (Stephenson 1976; Srnka 1976), known to be the only measurable contributor to the external magnetic field of Mars (Acuña et al. 1999). Mercury's small obliquity and spin-orbit resonance lead to stable, large-scale latitudinal and longitudinal variations in insolation and thus to similar geographical variations in the depth to a specific Curie isotherm at a given time in the planet's thermal history. The crustal fields imparted by a steady internal field during the time that the outer crust cooled through the Curie temperatures of any magnetic minerals present would give rise to an external field with a dominant dipole term and specific relative magnitudes for multipolar components (Aharanson et al. 2004).

Finally, the modest planetary magnetic moment implies both that the conductive core is much larger relative to the magnetosphere than for any other planet of the Solar System and also that the magnetic signatures of induction currents flowing in the core are larger relative to the background core dynamo field. Thus, inductive fields may contribute as much as  $\sim 10\%$  to the surface field, depending on variations in the external field (Grosser et al. 2004; Glassmeier et al. 2007a). Since both the external and induced fields are imposed on the core, there may be a feedback such that these external fields act as seed fields for the dynamo over long timescales (Glassmeier et al. 2007b). It is therefore of great interest to identify signatures of induced fields.

## 2.2 External Current Systems

Because the contribution of the magnetospheric current systems to the total observed magnetic field even near the surface is comparable to the field from internal sources, quantitative understanding of the electric currents associated with solar wind interaction with Mercury's magnetic field is critical to the study of the internal field (Russell et al. 1988). Magnetopause and magnetotail cross-tail currents are known to be present at Mercury. Of these the magnetopause current is the better known, because the magnetopause boundary location can be specified with reasonable accuracy (Slavin and Holzer 1981; Russell et al. 1988) and also because the intensity of the current can be specified from first principles (Tsyganenko 1995).

The cross-tail current is less well understood at Mercury because of its apparent proximity to the planetary surface. Earth-analog models place at least some of the cross-tail current below the surface of the planet (Korth et al. 2004; Tsyganenko and Sitnov 2005). The actual proximity of the tail current to the planet and the down-tail gradient are not well known. Mariner 10 flyby data suggest that the tail current is sufficiently intense close to the planet to reduce the net field to less than one-third of the internal field as close as 700 km from the surface (Ness et al. 1975). For this reason the tail current is one of the key features of magnetosphere magnetic field models customized for Mercury (Giampieri and Balogh 2001; Alexeev et al. 2008).

Prior to the first MESSENGER flybys the presence of local plasmas in Mercury's magnetosphere was inferred from variations in the magnetic field (Christon 1987). We now know that protons are found close to the planet within  $0.5R_M$  altitude (where  $R_M$  is Mercury's radius), evidently with sufficient densities to depress the local magnetic field by tens of nT

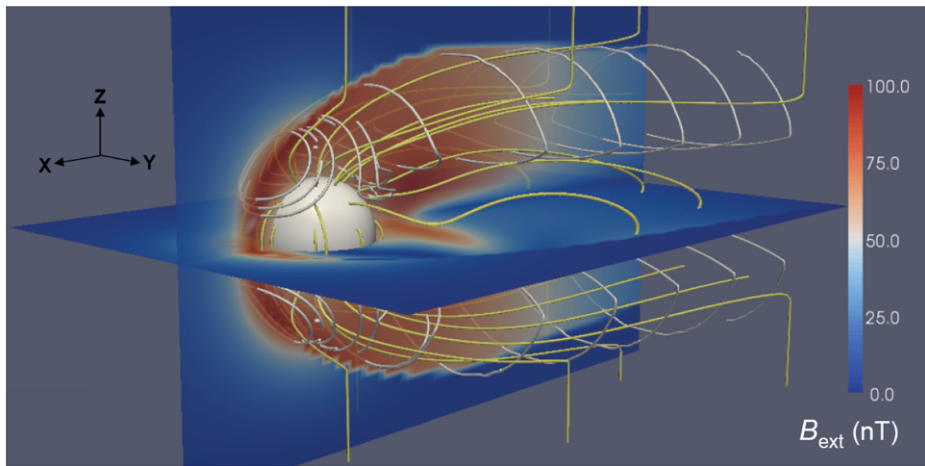


**Fig. 1** Magnetic field lines (yellow), current density traces (white), and external magnetic field magnitude (color bar) for the TS04 magnetic field model scaled for Mercury. For the case shown the TS04 model was evaluated for a purely southward IMF of magnitude 10 nT and a solar-wind ram pressure of 20 nPa. An axially aligned dipole with a moment of  $250 \text{ nT} \cdot R_M^3$  was used for the planetary field. The model is shown in Mercury-solar-orbital (MSO) coordinates, with  $X$  positive toward the Sun,  $Z$  positive normal to the orbital plane, and  $Y$  completing the right-handed system

(Anderson et al. 2008b; Zurbuchen et al. 2008). The flyby encounters do not allow a comprehensive specification of the plasma distributions, but initial results are at least qualitatively consistent with numerical simulations (Trávníček et al. 2007, 2009) strongly indicating that the plasma distributions at Mercury are very different from those of any other magnetosphere. It is therefore to be expected that the current systems due to plasmas within the magnetosphere will be different at Mercury from those at other magnetospheres.

In addition to these factors, the solar wind and interplanetary magnetic field (IMF) imposed on Mercury's magnetosphere are variable and change both the intensity and configuration of the magnetopause and tail currents and presumably also alter the internal plasma distribution (e.g., Luhmann et al. 1998). The reconfiguration timescale for Mercury's magnetosphere is on the order of tens of seconds to a minute (e.g., Slavin et al. 2007), far shorter than either the transit time of any of the flyby encounters conducted to date or the period of any orbit about the planet. Identification of the appropriate solar wind and IMF conditions to use in attempts to model and correct for the externally generated magnetic fields is an important problem that may ultimately limit knowledge of the internal field structure derived from observations. Nonetheless, a simple extension of conditions of the IMF during the previous solar wind pass should provide approximately a factor of 10 increase in analysis sensitivity over ignoring the external field altogether (Korth et al. 2004).

To illustrate the critical role of the external fields, in Fig. 1 we show the magnetic field and external currents in the Earth-analog TS04 model (Tsyganenko and Sitnov 2005) scaled to Mercury (Korth et al. 2004) and depicted in Mercury-solar-orbital (MSO) coordinates. The fundamental topology of the magnetosphere is evident in this figure. The magnetopause Chapman-Ferraro currents are the closed circular loops on the dayside magnetopause around the magnetic cusps. The dayside is highly compressed, and the magnetic field in the polar regions is topologically linked to the lobes of the magnetotail, which are separated by the cross-tail current. The tail current system flows over the northern and southern lobes and closes across the middle of the tail, flowing from dawn to dusk. In this model the external

field contributes over 100 nT to the total field over large regions of space, especially close to the planet. Its accurate specification is obviously crucial to an accurate specification of the planetary magnetic field.

### 3 Observations from the MESSENGER Flybys

#### 3.1 Magnetic Field Observations Overview

Portions of the trajectories from which magnetic field observations were used for internal field analysis, projected to Mercury body-fixed coordinate latitude and longitude, are shown in Fig. 2. The trajectories include Mariner 10 flybys I and III (M10-I and M10-III), the first two MESSENGER flybys (M1 and M2), and the trajectory planned for the third MESSENGER flyby (M3). The third Mariner 10 encounter provided the only observations to date at high latitudes, and the second MESSENGER flyby yielded the first magnetic field observations from the planet's western hemisphere. The third MESSENGER flyby will cover nearly the same longitudes as M2.

The M1 and M2 flyby trajectories are shown in Fig. 3. Nominal magnetopause and bow-shock boundaries are also shown (Slavin et al. 2009a). For M2 the MESSENGER spacecraft passed inbound farther tailward and outbound somewhat later in the morning than for M1. Magnetic field data for 110 minutes spanning each encounter are depicted in Figs. 4 and 5. From top to bottom the panels show: the field magnitude; the polar angle,  $\theta$ ; the azimuth angle,  $\varphi$ ; and the 1–10-Hz passband fluctuation amplitude in nT. The maximum magnetic field was nearly the same for both encounters, 159 nT for M1 and 158 nT for M2, despite the  $\sim 180^\circ$  longitude separation (Fig. 2). As expected from the differences in the trajectories, MESSENGER's inbound bow-shock crossing for M2 occurred earlier relative to closest approach than for M1.

The data for the inbound portions of the passes indicate that for M1 the spacecraft entered into the cross-tail current sheet (CS), whereas for M2 the spacecraft entered directly into the southern magnetic tail lobe (TL). For M1 the field between the magnetopause (MP) and CS remained nominally northward, indicating that the spacecraft was near the center of the cross-tail current. At CS the field began to rotate away from northward to anti-sunward, implying passage from the current sheet into the southern magnetotail lobe, where the field

**Fig. 2** Trajectories of Mariner 10 flybys M10-I and M10-III and MESSENGER flybys M1, M2, and M3 plotted in Mercury body-fixed (MBF) coordinates. Longitude is positive to the east

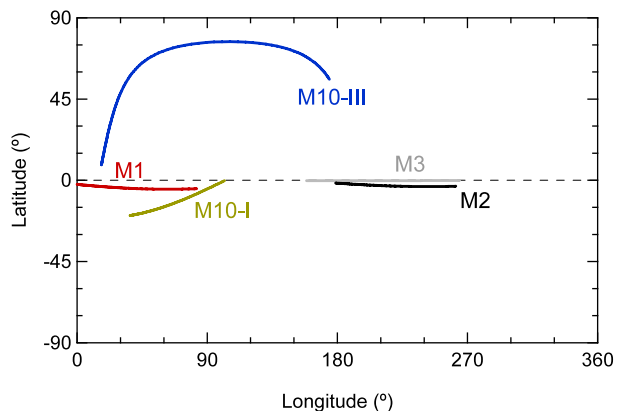
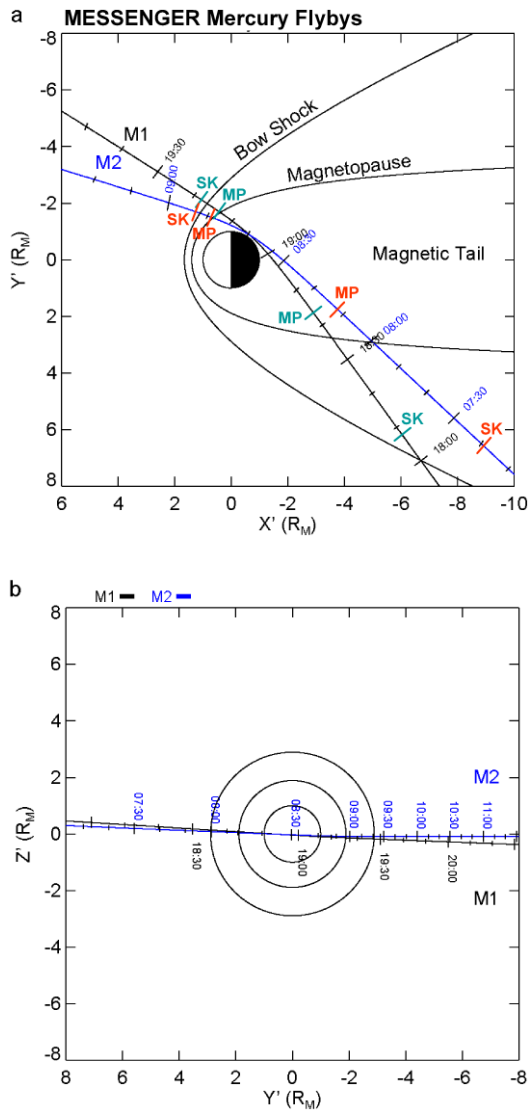


**Fig. 3** Trajectories of the first and second MESSENGER flybys of Mercury, denoted M1 and M2, respectively, in MSO coordinates. *Primes* indicate that the system accounts for aberration in the solar wind flow due to Mercury's orbital motion. Panel (a) shows the view in the  $X'-Y'$  plane looking down from the north, and panel (b) shows the view in the  $Z'-Y'$  plane looking toward the Sun. Nominal magnetopause and bow-shock boundaries are shown for the equatorial ( $Z' = 0$ ) plane in panel (a) and the  $X' = 0$  plane in panel (b). The observed bow shock (SK) and magnetopause (MP) crossings are marked on panel (a) in green for M1 and red for M2



is anti-sunward. For M2, by contrast, the field was strongly anti-sunward immediately following the inbound MP, indicating direct entry into the magnetotail southern lobe.

The rotation of the field from anti-sunward to northward began at TL for M1 and M2, indicating the transition from the magnetotail lobe to the region dominated by the planet's internal field. For M1 the maximum field magnitude occurred shortly after closest approach (CA), and for M2 the maximum field occurred slightly prior to CA. For both flybys on the outbound leg a relatively sharp drop in field magnitude without a change in direction occurred approximately five minutes prior to MP. We term this transition a dayside boundary layer and denote it as BL. For purposes of estimating the internal planetary magnetic field, the appropriate data ranges are taken from TL to BL because these represent data dominated

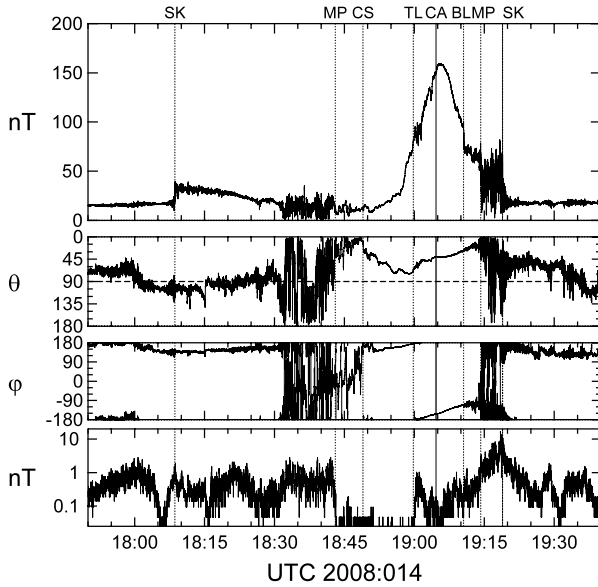


**Fig. 4** Magnetic field data from the first MESSENGER flyby presented in MSO coordinates. From top to bottom the panels show: the field magnitude; the polar angle,  $\theta$ , where  $\theta = 0^\circ$  is northward; the azimuth angle,  $\varphi$ , where  $\varphi = 0^\circ$  and  $90^\circ$  are sunward and duskward, respectively; and the 1–10-Hz band-pass fluctuation amplitude. Magnetic field vectors were sampled every 0.05 s, and the 1–10-Hz band-pass amplitude was evaluated on-board every 1 s from the 0.05-s data. Magnetic boundaries are labeled as follows: SK for bow shock; MP for magnetopause; CS for the tail current sheet; TL for transition out of the tail lobe; CA for closest approach; and BL for entry into a boundary layer

by the planetary field; these ranges do not include observations in the lobes or inside the dayside boundary layer.

For M1 the magnetic field following the outbound MP crossing was somewhat northward both in the magnetosheath and for about 20 minutes after the bow-shock crossing (SK) in the interplanetary medium. For M2, however, the magnetosheath field was strongly southward between MP and SK for both the inbound and outbound portions of the encounter and was southward in the interplanetary medium both before and after the encounter. Thus, the IMF at Mercury was northward as of the outbound passage on M1, whereas for M2 the IMF was likely to have been southward throughout the encounter.

Evidence of magnetospheric dynamics indicates significant differences in Mercury's magnetosphere between M1 and M2. During M1 MESSENGER detected signatures of a modest flux transfer event just outside the inbound tail magnetopause crossing and Kelvin-Helmholtz vortices shortly after the inbound crossing, indicating the occurrence of reconnection and boundary waves analogous to those observed at Earth (Slavin et al. 2008). The first flyby also revealed a boundary layer within and adjacent to the outbound magnetopause crossing, but there were no indications of reconnection on the outbound magnetopause crossing (Anderson et al. 2008b; Slavin et al. 2008). By contrast, data from the second MESSENGER flyby show intense reconnection signatures in the vicinity of both inbound and outbound magnetopause passages (Slavin et al. 2009b). These include flux ropes and a series of traveling compression regions on the inbound leg and two strong reconnection events on the outbound leg, one an intense flux transfer event with a core field stronger than the maximum field observed within the magnetosphere (Slavin et al. 2009b).

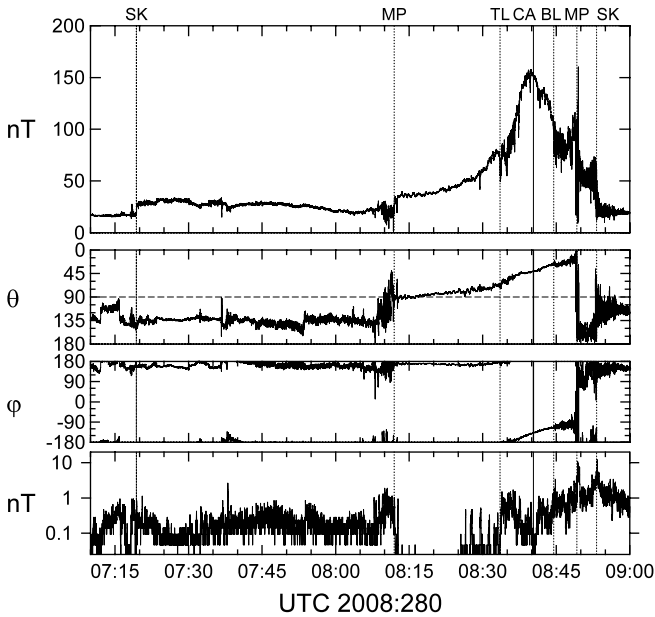


**Fig. 5** Magnetic field data from the second MESSENGER flyby in the same format as Fig. 4. The Magnetometer operation and sampling were identical to that for the data shown in Fig. 4. Magnetic boundaries are labeled as in Fig. 4 except that there is no CS boundary in this case

### 3.2 Plasma Observations

In addition to the Magnetometer, MESSENGER carries a plasma sensor, the Fast Imaging Plasma Spectrometer (FIPS), which measures ions in situ over the energy range from tens of eV to 13.5 keV as part of the Energetic Particle and Plasma Spectrometer (EPPS) instrument (Andrews et al. 2007). The FIPS detector provides coverage over an approximately  $1.4\pi$ -steradian solid angle, although the useful field of view is somewhat lower because the instrument is obstructed by the spacecraft sunshade and one of the spacecraft's two solar panels. The center of the field of view is somewhat sunward of the perpendicular to the spacecraft-Sun direction. Plasma flow away from the detector look direction will not be measured, and hence in many situations FIPS will record only the high-velocity, super-thermal portion of the plasma distributions. One must therefore always be mindful that differences in flow direction can lead to variations in the FIPS data that are not indicative of corresponding changes in plasma density or temperature.

FIPS proton observations are shown along with expanded views of the magnetic field data near CA in Figs. 6 and 7. The second panels of Figs. 6 and 7 show FIPS proton energy spectra integrated over the FIPS field of view to yield a phase-space density that is normalized to the maximum value in the plot. The third panels of Figs. 6 and 7 show the time series of total proton counts summed over all energies and angles. The phase-space density normalization is different for M1 and M2, but the proton counts are in absolute units, counts per 10 s.

The proton data change at all of the transitions noted from the magnetic field data. At TL for M1, the proton fluxes below 1 keV decreased in approximately two steps, the first at 18:58 UTC prior to TL when the field magnitude began to increase more rapidly, and then

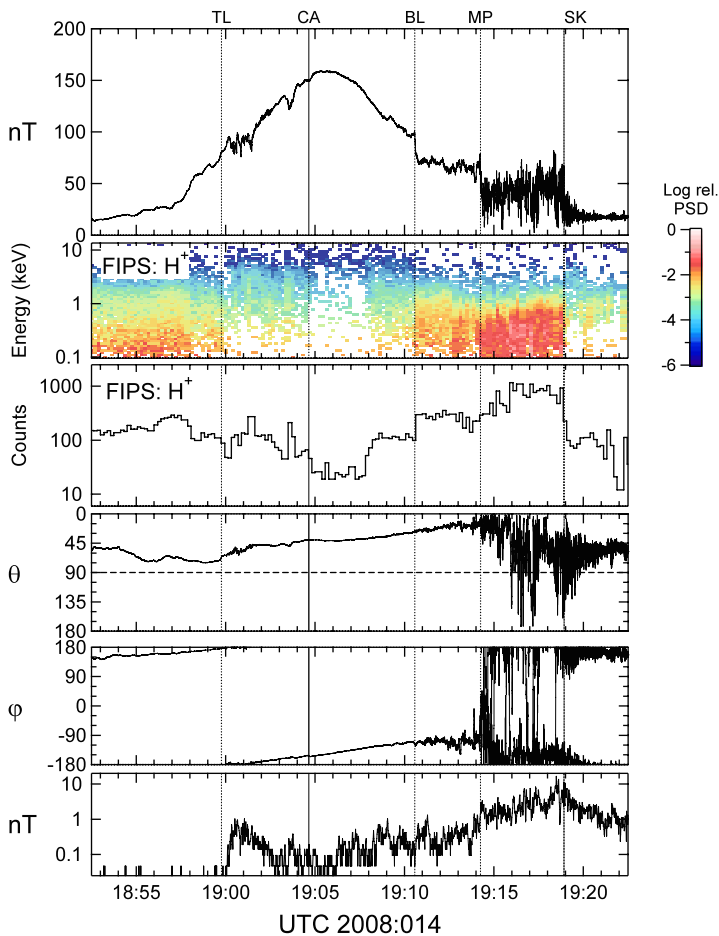


**Fig. 6** Magnetic field data together with proton observations from FIPS for 30 minutes spanning the M1 encounter. Transition labels are the same as in Fig. 4. Data between points TL and BL were selected for estimating the internal magnetic field. In addition to the magnetic field data, which are re-plotted in expanded view from Fig. 4, the FIPS proton data show phase-space density (PSD) normalized to the maximum in the interval in the *second panel* and the summed proton FIPS counts in each 10-s integration in the *third panel*

again at TL when the lower-energy fluxes dropped to near the detection threshold. The presence of protons at hundreds of eV prior to TL is consistent with spacecraft residence near the cross-tail current sheet and suggests that the spacecraft remained in the tail plasma sheet until the point labeled TL. For M2 the proton fluxes were very low until TL, consistent with the interpretation that the spacecraft entered directly into the southern tail lobe where densities are expected to be low. Thus, for M2 the TL transition corresponds to the appearance of protons above  $\sim 1$  keV in the FIPS data.

Changes in the proton count rates and/or energy spectra occur at the boundary layer, magnetopause, and shock crossings on the outbound legs of both flybys. An increase in the FIPS protons at BL occurred in both cases, though it was greater for M1 than M2. The strong increase in protons at energies below 1 keV at the outbound magnetopause is obvious in both flybys as is the subsequent decrease in signal at the outbound shock crossing. In the

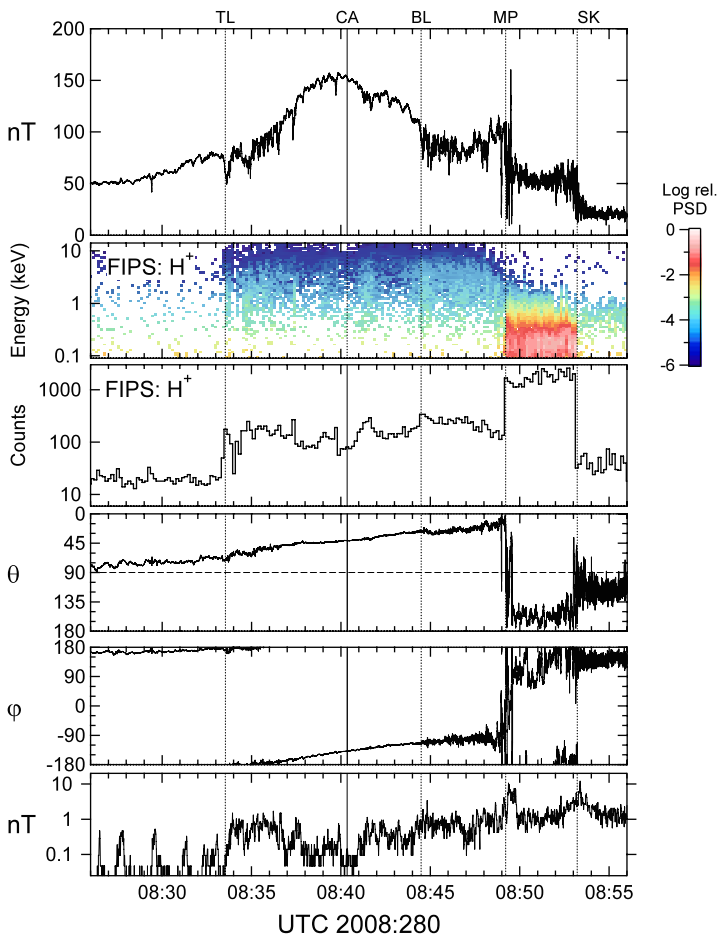


**Fig. 7** Magnetic field data together with proton observations from FIPS for 30 minutes spanning the M2 encounter. Transition labels are the same as in Fig. 5. Data between TL and BL were selected for estimating the internal magnetic field. The panels are shown with the same format as in Fig. 6

solar wind just upstream of the bow shock, FIPS did not observe the incident solar wind flow but rather protons reflected upstream from the shock. The changes in the protons therefore correspond with the transitions identified in the Magnetometer data and support the choice of data between TL and BL for analysis of the internal magnetic field. Significantly, they also reveal that  $\sim$ keV-proton populations permeate Mercury's magnetic field environment near the equator as close to the surface as the M1 and M2 closest approach altitudes of 200 km.

### 3.3 Implications of Plasma and Solar Wind Environment for Internal Field Estimates

We now focus on the intervals used for estimating the planetary field, between TL and BL in Figs. 6 and 7, paying particular attention to signatures in the data reflecting processes other than internal field sources. We note that both encounters showed sporadic decreases in the field magnitude without significant changes in field direction. The magnitude was generally

more variable for M2 than for M1. For M1 there was one particularly prominent decrease in the magnetic field of about 10 nT about 1 minute before CA. This decrease in magnetic field magnitude corresponded to an increase in the FIPS proton count rate by a factor of three, suggesting that the drop in magnetic field was associated with a plasma structure. Prior to this point, from about 19:00 to 19:02 UTC, the magnetic field magnitude was somewhat variable, with multiple downward spikes of  $\sim 10$  nT.

The field magnitude close to the planet was more variable for M2 than for M1. Nearly coincident with TL on M2 there was a decrease of  $\sim 25$  nT or nearly one third in the field magnitude coincident with a factor of 5 increase in the proton count rate. The field magnitude varied erratically by up to 20 nT from TL to 18:36:30 UTC. Additional isolated decreases of  $\sim 25$  nT at 08:37:30 UTC and again of  $\sim 15$  nT just before 08:40 UTC both coincided with spikes in the proton count rate. A broader local minimum in the field near 08:41:30 UTC was coincident with a correspondingly broad increase in the FIPS proton count rate. The prevalence, intensity, and correlation of these short-timescale magnetic field decreases for both M1 and particularly M2 suggest that the magnetic field even close to the planet is affected by local plasmas and currents corresponding to the pressure gradients in the plasma. Thus, the standard assumption that the volume near the planet is free of local currents (e.g., Backus 1970) does not hold even within a few hundred kilometers of the surface.

There is another difference in character of the magnetic field observed during M2 relative to M1. Other than the relatively sharp field decreases discussed above, the magnetic field between TL and BL on M1 was fairly smooth, whereas for M2 the magnetic field exhibited a train of  $\sim 10$ -nT modulations each lasting  $\sim 10$  to 20 s. The modulations were most evident after CA, when three or four of these oscillations occurred from  $\sim 08:42$  to  $08:44$  UTC, in marked contrast to the smooth field gradient during M1 between CA and BL. As discussed above, the IMF conditions for M2 and M1 were different. The IMF was southward before and after MESSENGER's transit through the magnetosphere for M2, whereas it was northward at the outbound M1 magnetopause crossing. The M2 encounter displayed signatures of intense magnetic reconnection dynamics both in the tail and at the magnetopause with a repetition interval of about 20 to 30 s (Slavin et al. 2009b). The spike in the magnetic field magnitude just after MP, at  $\sim 08:49:30$  UTC for M2, is the strong flux rope reported by Slavin et al. (2009b). It is possible that the quasi-periodic variations in magnetic field intensity during the M2 pass near the planet are also signatures of this dynamic interaction with the magnetized solar wind plasma.

The inference that local plasmas and the dynamic solar wind interaction make significant contributions to the magnetic field close to the planet has direct implications for estimates of the planetary field from the flyby data. Clearly, the identification of magnetic signatures due to local plasmas and perhaps magnetospheric dynamics implies that crustal signatures will be difficult if not impossible to distinguish from local plasma or dynamic signatures. Moreover, the MESSENGER observations imply that local plasmas and corresponding local magnetization currents are present close to the planet. These local plasmas contribute up to 30-nT signals in the volume of space from which the near-planet magnetic field data were obtained. Thus, one cannot assume that the data were obtained in a current-free volume, and spherical harmonic solutions for the external field must be used with caution because they are strictly applicable only to curl-free fields. We emphasize that the short time-scale plasma signatures indicate the presence of plasma even though we do not attempt to model the short-wavelength signatures of these local plasma phenomena. Large-scale external currents are strongly indicated by the presence of local plasmas, and these long-wavelength signatures are of concern for the spherical harmonic inversion analyses.

In addition, variations of 10 to 20 nT are present that are likely due to dynamic processes and do not reflect spatial structures. That these signatures are found on the M2 pass for which the magnetopause crossings gave evidence for strong, episodic reconnection dynamics suggests that these quasi-periodic oscillations could be due to the dynamic interaction of the magnetosphere with the solar wind. It appears that these signatures permeate the system, and therefore estimates of Mercury's magnetic field will necessarily be subject to residuals of this order. Obviously, fitting these signals as if they were spatial structures in the internal field would be incorrect.

In estimating the internal magnetic field structure of Mercury one must therefore adopt an approach that recognizes the intrinsic limitations that the physical system imposes. First, although there are several obvious common elements between Mercury's magnetosphere and those of other planets, particularly Earth, Mercury's magnetosphere is unlike any system explored to date in many key respects that prevent us from accurately specifying the external field (e.g., Glassmeier 2000). Thus, we use available knowledge to correct for the portions of the external field in which we have the most confidence and then examine the data for signatures of additional current systems that must be considered specifically for the Mercury system. As discussed below, simulation results play a role in guiding this analysis. Second, given the intrinsic limitations of the data in hand and the challenges presented by the Mercury system, the use of higher-order terms in estimating the internal field must be treated with caution. For this discussion, we adopt the view that higher-order terms should be invoked if there is a reason, supported either from observations or simulations, to exclude an external or local current structure as accounting for the observations. Given the nature of the external and local sources of magnetic field, we judge that this posture is necessary to avoid drawing erroneous conclusions about Mercury's internal field.

## 4 Critical Assessment: External Field Treatment

For Mercury, the importance of external and local sources of magnetic fields for accurate assessment of the internal planetary field is surpassed perhaps only by the difficulty in deriving accurate representations of these external and local sources. Moreover, because of their importance and the evidence for local sources of current even at the lowest altitudes, it is particularly important when including external field corrections for Mercury to be guided by the physics of the magnetosphere and its solar wind interaction. There are three techniques that can be used to estimate the external field. The first is to use a potential formalism that treats the external field much as the internal field, but due to sources outside the sampled volume. The second applies analytical empirical models that use a set of specified current systems that are constrained empirically in location and intensity by observations. Finally, advances in computational capability allow one to contemplate the use of physics-based simulations that obtain the magnetospheric and plasma structures and currents from numerical simulation of fluid and/or particle equations of motion.

### 4.1 Spherical Harmonic Fitting

One approach commonly used to estimate external field contributions is to use spherical harmonic analysis (SHA) for sources outside the sample volume (Backus 1970; Menke 1989). While this approach is convenient, it makes the implicit assumption that the sample volume is current-free. This cannot be safely assumed for Mercury. Moreover, even with four flybys, the sampling of the magnetospheric volume at Mercury is quite limited. All

of the passes are nightside cuts through the system, with M10-I, M1, and M2 passing near the equator and M10-III over the northern pole. The addition of the M2 data require that the external and internal fields are treated in MSO and Mercury body-fixed (MBF) coordinates, respectively, in the same singular value decomposition (SVD) inversion (Uno et al. 2009). Although the M2 trajectory sampled a new range in planetary longitude (Fig. 2), the path in magnetospheric coordinates was similar to that for M1 (Fig. 3). Because the flyby trajectories in MSO coordinates are similar, the constraints on the external currents provided by these data are not particularly robust. Estimates of the external field using SHA yield quite different solutions depending on the choice of maximum spherical harmonic degree for the external field and whether each flyby is considered to have different external fields (Uno 2009). These considerations together with the limitation that the region is not current-free make it difficult to judge the validity of SHA external field solutions. For this discussion, aimed at distinguishing those aspects of Mercury's magnetic field structure that are reasonably robust from those requiring additional study, we choose not to focus on the spherical harmonic approach in dealing with the magnetic field from external sources.

#### 4.2 Magnetospheric Current Models

Fortunately there are fundamental similarities in primary current systems of planetary magnetospheres (cf. Parks 1991, and references therein). The magnetopause and magnetotail currents are necessary consequences of the interaction of the supersonic solar wind with the planetary magnetic field, and all planetary magnetospheres in the solar system have these current systems. The magnetopause current system, or Chapman-Ferraro current layer, separates the magnetic field of the planet from the solar wind environment. For the magnetized planets of our Solar System, the solar wind flow speed is higher than the fast magnetosonic wave speed in the solar wind plasma, so a shock front forms upstream of the magnetopause where the solar wind flow decelerates at a shock bow wave and then diverts around the magnetic obstacle of the planetary field according to magnetohydrodynamics. These processes are generally understood, both observationally and theoretically. Given the shape of the magnetopause boundary and an approximate estimate of the planetary magnetic field (e.g., Sibeck et al. 1991; Shue et al. 1998), one can calculate the magnetopause current and the resulting externally produced magnetic field from first principles (Tsyganenko 1995; Tsyganenko and Sitnov 2005).

The magnetotail current system is the second primary current system directly implied by the structure of the magnetosphere and common to all planetary magnetospheres in the solar system (cf. Lui 1987, and references therein). The north and south polar magnetic flux of the planet is swept in the anti-sunward direction by the solar wind flow to form a pair of magnetic lobes (cf. Fig. 1). In the lobe connected magnetically to the southern magnetic pole, the magnetic field is directed toward the planet while in the other lobe the field is directed away from the planet and is linked to the northern magnetic pole. This configuration requires that there be a current flowing across the magnetotail between the lobes approximately bisecting the magnetotail. For Mercury the south magnetic pole is in the north, so the magnetic field is sunward (anti-sunward) in the lobe magnetically linked to the northern (southern) hemisphere.

The two-lobe magnetotail forms an approximately cylindrical structure that is observed to extend at least 30 times farther in the anti-sunward direction than the sub-solar magnetopause standoff distance measured from the planet center. The magnetotail diameter and the precise location of the cross-tail current sheet both vary between different systems. For systems with a significant tilt between the planetary orbital plane and the magnetic dipole

axis, the cross-tail current will be displaced out of the orbital plane toward the pole that points sunward. While all magnetospheres have a magnetotail and a cross-tail current, the north-south location, tilt, intensity, extension toward the planet, and dynamics vary.

Because the size of a magnetosphere scales directly with the planetary dipole moment, one can use empirical models obtained from Earth, for which we have the most in situ observations, to scale quantitatively to other systems (e.g., Luhmann et al. 1998). This scaling applies best for the magnetopause currents, whose location and intensity can be most accurately specified. The magnetotail currents, though certain to exist, are less reliably scaled with this approach. But one can at least use our present estimates of these currents for comparison with the Mercury system.

Other current systems have been identified but are not universally present. Currents associated with internal plasma distributions, e.g., Earth's ring current, or with magnetospheric convection, e.g., Earth's Birkeland and ionospheric currents, vary markedly among systems. For Mercury, we anticipate that the Earth analogy breaks down completely with respect to the ring, Birkeland, and ionospheric currents (Glassmeier 2000). The ring current depends on closed particle drift trajectories around the planet, but Mercury's magnetosphere is so small relative to the planet that no such drift trajectories are expected (Russell et al. 1988). The absence of an ionosphere at Mercury means that Earth analogs for field-aligned currents, which close in the ionosphere, may not apply at Mercury (Slavin et al. 1997; Ip and Kopp 2004).

There are two alternatives for estimating Mercury's external currents with analytical models. The first is to use those portions of Earth models that we have confidence apply to Mercury, namely the magnetopause and tail currents, and scale the models to Mercury (e.g., Luhmann et al. 1998; Korth et al. 2004). The second alternative is to develop analytical and empirical models unique to Mercury (Giampieri and Balogh 2001; Alexeev et al. 2008). Further development of these Mercury models is essential to take full advantage of data to be obtained from orbit around Mercury, first by MESSENGER (Solomon et al. 2007) and then by BepiColombo (Balogh et al. 2007). However, the reliability of these models depends critically on the available data for the Mercury system, which at present are quite limited. We use an Earth analog as a first step in the analysis to guide the identification of additional currents unique to Mercury.

#### 4.3 Physics-Based Simulations

Numerical simulations of Mercury's magnetosphere can inform the derivation of the internal planetary magnetic field in at least two ways. First, they can be used to guide the analysis and interpretation of observations and in that way assist in identification and specification of processes and structures unique to Mercury. Second, they may find application in the inversion of observations to identify higher-order structure in Mercury's magnetic field. This use has already found application in the analysis of the Ganymede system embedded in the Jovian magnetosphere (Jia et al. 2008).

Advances in computational speed have opened new opportunities for first-principles simulations of space plasma systems, and the Mercury magnetosphere system has received particular attention. The fluid approximation using the formalism of magnetohydrodynamics (MHD) has been applied to Mercury with considerable success (e.g., Ip and Kopp 2002). Other investigators have applied a hybrid fluid-kinetic formalism in which kinetic particle simulations are used for ions while the electrons are treated as a fluid (e.g., Trávníček et al. 2007). Fluid MHD simulations offer the advantage of speed and extensive heritage in application to a range of systems, while the hybrid simulations include particle transport

processes that may be critical to the Mercury system (e.g., Baumjohann et al. 2006). There is value in applying independent simulation codes using different approaches to the same system. Comparing results from the MHD and hybrid simulations may allow one to identify which processes can be explained from a purely fluid perspective and which depend on ion kinetic processes.

Simulations have already informed our understanding of Mercury's magnetotail and distributions of plasma within the magnetosphere. Both the hybrid and fluid simulations show that Mercury's small magnetic field leads to incidence of solar wind plasmas on the surface in broad regions around magnetic cusps and in equatorial regions on the night side of the planet where solar wind plasma "precipitates" onto the surface (Ip and Kopp 2002; Trávníček et al. 2007, 2009). The hybrid simulations indicate that solar wind plasmas permeate Mercury's magnetosphere even to very low altitudes in the cusp and equatorial regions at least in part following entry in the cusps followed by conventional drift on closed field lines (Trávníček et al. 2007). This process appears to result in structured inclusions of solar wind plasma at very low altitudes, down to the surface, within a planetary radius and near the equator on the nightside (Trávníček et al. 2007). These results are consistent with the MESSENGER magnetic field and plasma observations discussed above. The hybrid simulations also reveal displacement of the cross-tail current toward the north for the negative IMF  $B_x$  conditions for M1 and M2 (Trávníček et al. 2007, 2009). Thus, the simulations are already providing a conceptual framework to assist in the interpretation of the available observations.

## 5 Internal Field Estimation

The MESSENGER observations from the first and second flybys provide the first additional data on the planetary field since the Mariner 10 encounters, and the M2 encounter gave us our first observations of the magnetic field in the western hemisphere of the planet. The MESSENGER encounters are particularly useful because relatively unperturbed data were obtained throughout each encounter, in contrast to the first Mariner 10 flyby, for which a magnetospheric disturbance occurred just after closest approach so that only the inbound portion of that pass can be used in internal field estimations (Ness et al. 1974; Christon 1987). Moreover, closest approach for both MESSENGER flybys was at 200 km altitude, lower than the Mariner 10 encounters. Nonetheless, the third Mariner 10 encounter observations are perhaps the most central to our understanding of Mercury's magnetic field since this flyby offers the only in situ observations to date from the polar regions of the planet.

### 5.1 Moment Inversions

Following the M1 encounter, Anderson et al. (2008b) assessed the internal field and showed that a pure-dipole representation underestimates the field over the pole while overestimating it near the equator. They compared results for different approaches to correcting the external field and concluded that the planetary moment is most likely in the range 230 to 290 nT- $R_M^3$ . The residuals remained relatively high, 15 to 30 nT, relative to typical planetary moment inversions, but consistent with the signatures of dynamics and local currents. Subsequent analyses assessed the higher-order internal field structure that the data may imply, revealing that the planetary field appears to be dominated by the  $g_1^0$  term (Uno et al. 2009), where  $g_n^m$  is the spherical harmonic coefficient for the  $n$ th order and  $m$ th degree. A search for specific

**Table 1** Inversion results for Mercury’s magnetic field using observations from Mariner 10 flybys I and III and MESSENGER flybys M1 and M2

Internal model	External field	$g_1^0$	$g_1^1$	$h_1^1$	$g_2^0$	$g_2^1$	$g_2^2$	$h_2^1$	$h_2^2$	Residual (nT)	Condition number
1 Dipole	None	-216	-6	14						42	2
2 Dipole	TS04	-240	-1	5						29	2
3 Dipole <sup>a</sup>	SHA	-249	-12	16						30	7
4 Quad.	None	-173	-7	15	-108	-9	-1	16	-17	19	3
5 Quad.	TS04	-213	-4	7	-66	9	4	5	-4	14	3
6 Quad. <sup>a</sup>	SHA	-182	-15	9	-108	10	2	6	-15	15	12
7 Reg. <sup>b</sup>	TS04	-222	12	2	-24	9	9	-6	8	24	n/a
External terms		$G_1^0$	$G_1^1$	$H_1^1$	$G_2^0$	$G_2^1$	$G_2^2$	$H_2^1$	$H_2^2$		
3 Dipole <sup>a</sup>	SHA	47	26	8	10	-15	-3	-2	-8		
6 Quad. <sup>a</sup>	SHA	7	-4	-15	-9	-9	-3	2	0.4		

All coefficients are in units of nT for spherical harmonic expansion with distance normalized to a mean Mercury radius. Quad. denotes quadrupole. The coefficients  $g_n^m$  and  $h_n^m$  are the cosine and sine spherical harmonic coefficients, respectively, of order  $n$  and degree  $m$  for the terms that decrease with radial distance, hence for the internal sources. The  $G_n^m$  and  $H_n^m$  are the cosine and sine spherical harmonic coefficients, respectively, for the terms that increase with radial distance, hence for the external sources (cf. Menke 1989)

<sup>a</sup>Results for the spherical harmonic analysis (SHA) treatment for the external field are from Uno (2009)

<sup>b</sup>Results for the regularized solution are from Uno (2009). The  $g_n^0$  terms in the regularized solution are as follows:  $g_3^0 = -2$ ;  $g_4^0 = -4$ ;  $g_5^0 = -5$ ,  $g_6^0 = 0$ ;  $g_7^0 = 1$ ;  $g_8^0 = 0$

crustal magnetic field signatures found that the perturbations near CA were not consistent with a crustal magnetization signature (Purucker et al. 2009).

The addition of the M2 data allows an assessment of long-wavelength longitudinal structure in the planetary field. Uno (2009) added the M2 observations to both spherical harmonic analyses in which internal and external fields were co-estimated using SVD (see Sect. 4.1) and to regularized inversions for the internal field after removal of external fields predicted by TS04. The regularized solution yields a dominantly dipolar field, aligned to within 5° of the planetary rotation axis. The results both for the SVD inversions and the regularized solution are summarized in Table 1 together with inversions added here for comparison. Here we add dipole and quadrupole SVD solutions that use either no external field correction or the TS04 external field correction.

The dipole fit results, from internal models 1 through 3 in Table 1, are very similar to previous results after M1 with the difference that the tilt of the dipole from the spin axis is now smaller. The Anderson et al. (2008b) dipole moment fit using the TS04 correction was 229 nT- $R_M^3$  with a tilt of 9°, and the SHA external field solution gave a moment of 247 nT- $R_M^3$  with a tilt of 12°. The new result using the same inversion, dipole with TS04 correction, gives a dipole moment of 240 nT- $R_M^3$  and a tilt of 1°. The SHA external field yields a dipole moment of 250 nT- $R_M^3$  and a tilt of 5°. Accounting for the external field even in these approximate ways reduces the residuals.

The results for higher-order terms, models 4 through 7 in Table 1, are also consistent with the previous analyses. The quadrupole solutions and the regularized degree and order

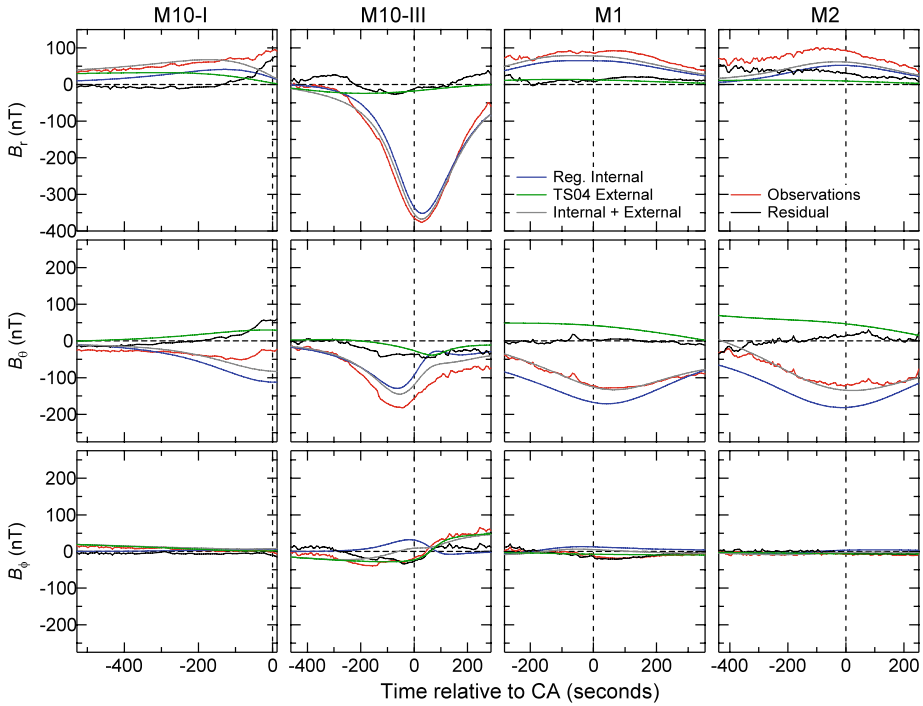


**Fig. 8** Overview of Mariner 10 and MESSENGER observations of Mercury’s magnetic field. Results are plotted in MBF coordinates: radial ( $B_r$ ), polar angle  $\theta$  ( $B_\theta$ ), and azimuth angle  $\phi$  ( $B_\phi$ ) versus time relative to closest approach (CA). Lines show observations (red), internal field model from regularized solution (blue), TS04 external field model (green), sum of the internal and external models (grey), and residuals (black). The span of magnetic field values plotted is 550 nT for all three components

8 inversion have lower dipole moments and a quadrupole moment with a magnitude 30% to 60% of the dipole. The quadrupole and regularized inversions that use data corrected for the TS04 external field have smaller higher-order terms than the other two quadrupole inversions. The sum of all  $g_n^0$  from  $n = 1$  to 8 for the regularized solution is  $-255$  nT, lower than the sum of  $g_1^0$  and  $g_2^0$  for the quadrupole solutions, 4, 5 and 6, which are  $-281$  nT,  $-271$  nT, and  $-290$  nT, respectively. The residuals for the higher-order fits are 10 to 15 nT lower than the external-field-corrected dipole inversions but are still between 7% and 11% of the dipole term. Note that the magnitude of the residuals for the regularized solution is determined by the weights used in the inversion, and these are conservative (i.e., large) reflecting mainly contributions from uncertainties in the external field correction and short wavelength signals (Sect. 3.3, and see Uno 2009; Uno et al. 2009).

### 5.2 Residuals: Initial Assessment

We now examine the inversions in detail to understand what features in the data lead to the quadrupole terms and identify the factors contributing to the residuals. The observations, external and internal models, and residuals are shown in Fig. 8 for the regularized solution, model 7, of Table 1. The data are shown in  $r-\theta-\phi$  MBF coordinates versus time in seconds relative to CA for each of the flybys. The residuals are shown in Fig. 9 in a similar format with the addition of the bottom row. The net model does a good job of representing the

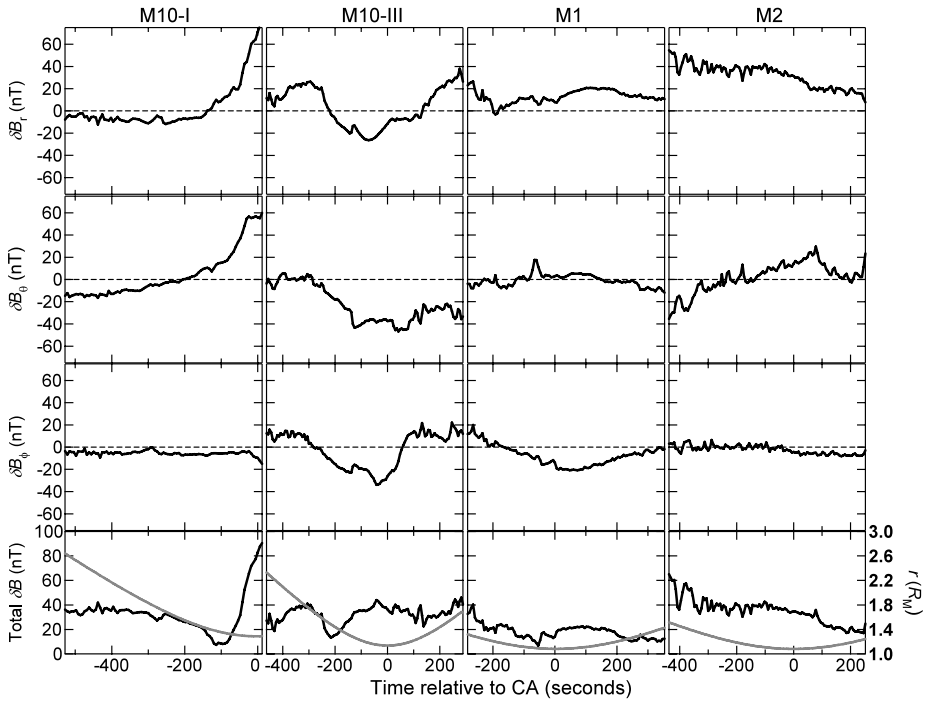


**Fig. 9** Magnetic field residuals in MBF spherical coordinates radial ( $\delta B_r$ ), polar angle  $\theta$  ( $\delta B_\theta$ ), and azimuth angle  $\phi$  ( $\delta B_\phi$ ), for the Mariner 10 and MESSENGER flybys. In the bottom row the residual magnitude ( $\delta B$ ) is plotted (left-hand axis) together with the planetocentric distance (right-hand axis). Residuals are evaluated relative to the regularized solution with the TS04 external field correction. Gray traces show spacecraft radial distance from the planet in units of planetary radii

dominant field components for M10-III, M1, and M2 but cannot fit the M10-I data near closest approach, for which the residuals are nearly 50 nT. In all cases, the TS04 model field is a slowly varying contribution and is everywhere less than  $\sim 60$  nT. The  $B_\phi$  results for M10-III give the appearance of a TS04 external field that reverses sign shortly after CA, but this is just a coordinate transformation from a uniform field into the azimuthal direction, which reverses as the trajectory crosses near the pole. The observed and modeled  $B_\phi$  for M10-I, M1, and M2 are quite small. Finally, we note that the M10-I  $B_r$  and  $B_\theta$  and the M10-III  $B_\phi$  residuals are largest near CA but that none of the other residuals are largest near CA. The largest residual for M10-I is  $\delta B_r$  near CA, but for M10-III the largest residual is in  $\delta B_r$ , about 300 s prior to CA, for M1 it is in  $\delta B_\theta$  also at the beginning of the interval about 300 s prior to CA, and for M2 it is in  $\delta B_r$ , more than 400 s before CA. The lack of dependence of the residuals on radial distance is also evident in the bottom row of Fig. 9, from which it is difficult to discern a correlation between radial distance and residual magnitude.

### 5.3 Residuals: Spatial Distributions

To illustrate how the data and trajectories are related we display the data using a different format in Fig. 10. The figure shows the observations in MBF coordinates (top panels) and the residuals from the dipole fit (bottom panels), model 1 of Table 1, to the data without making any external field correction, also in MBF coordinates. The trajectories are shown

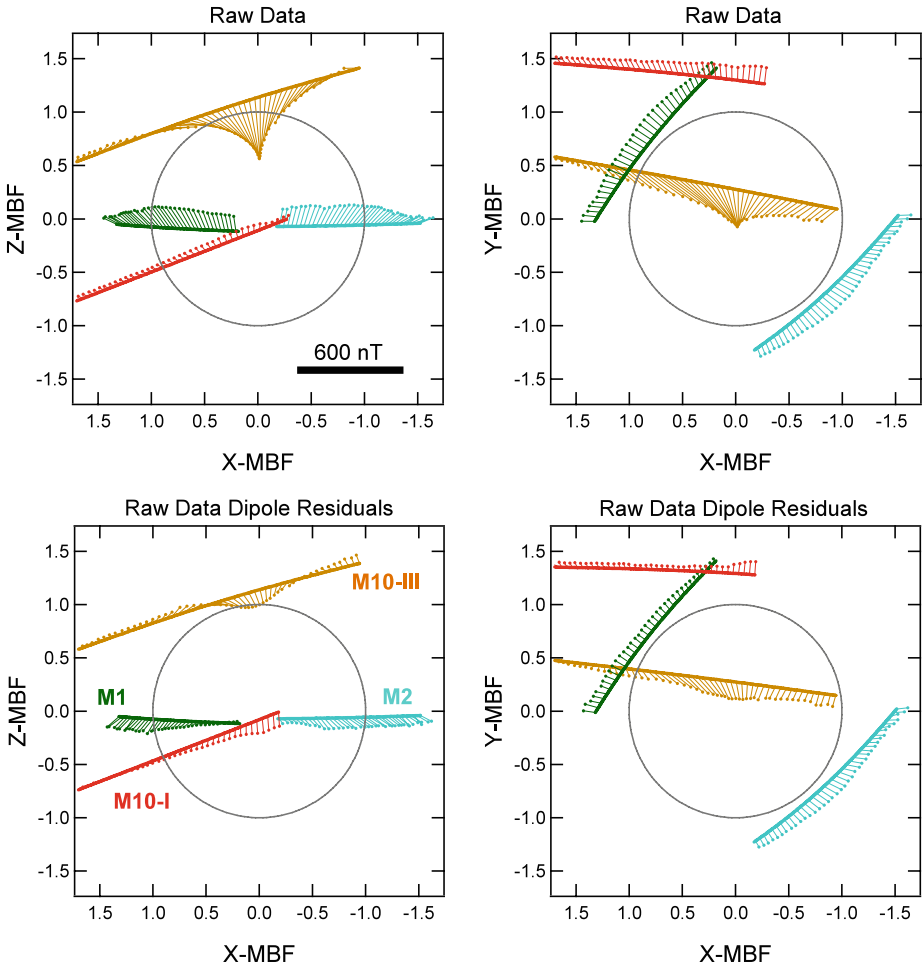


**Fig. 10** Overview of Mariner 10 and MESSENGER magnetic field data used for estimating the planetary internal magnetic field. Data and trajectories are shown in MBF coordinates. *Arrows* show the field measured at the point on the trajectory where the arrow originates on the trajectory. The field is projected onto the plane viewed, the  $X-Z$  MBF plane *on the left* and the  $X-Y$  MBF plane *on the right*. Color coding is as follows: Mariner 10 I (M10-I) is shown in *red*; Mariner 10 III (M10-III) is shown in *tan*; MESSENGER flyby 1 (M1) is shown in *dark green*; MESSENGER flyby 2 (M2) is shown in *light blue*. The *top panels* show the observations prior to any corrections for external or internal field sources. The *bottom panels* show the residuals relative to a centered dipole fit to the observations (model 1 of Table 1). The length of an arrow corresponding to 600 nT is indicated in the *top left panel*

in units of  $R_M$ , and the magnetic field data are shown as lines starting from the trajectory in the direction of the field projected onto the plane of the plot. The M10-III flyby data clearly show the magnetic field directed toward the planet over the pole but also have a significant horizontal field over the pole. The M1 and M2 data yield a northward-directed field near the equator but also show a radially outward field, as do the M10-I flyby data. The M10-I observed field is not strongly northward even near closest approach but is primarily radially outward, even nearest the planet.

The departure of the observations from the dipole, model 1 of Table 1, illustrates that a pure dipole cannot fit both the high-latitude and equatorial observations. The M10-III residual from the dipole is still southward over the pole, whereas the M10-I, M1, and M2 residuals are all southward, indicating that the dipole is too weak at the pole and too strong at the equator relative to the observations. The fact that the M10-III observations are too large relative to the M10-I and M1 observations near the equatorial plane to be explained in terms of a dipole was pointed out by Anderson et al. (2008b). The M2 observations confirm that the equatorial field is consistently low even for contrasting IMF conditions. From the  $Y-X$  plane view, we see that the radial equatorial field is present in the M10-I, M1, and M2 residuals and that the residual field at M10-III is still significantly horizontal.

To illustrate the role of the TS04 external field correction, in Fig. 11 we show the residuals for fits 1 and 2 of Table 1. The dipole fit residuals without and with the TS04 external field correction are shown in the upper and lower panels, respectively. Considering the  $Z-X$  plane first, we see that the external model reduces the southward residuals for M10-I, M1, and M2 but makes the field more northward at M10-III owing primarily to the stronger dipole moment of this fit. The signature of a residual southward field at M10-III near CA persists. In the  $Y-X$  plane, the horizontal residual at M10-III is much smaller in the TS04-corrected result, particularly before and after CA. The radial residuals in the equatorial plane are reduced but are still strong for M1 and M2.

Corresponding results of the higher-order internal models are shown in Fig. 12 where we plot the residuals for models 5 and 7 in the same format as Fig. 11. Comparing the TS04-corrected dipole solution (bottom panels of Fig. 11) and TS04-corrected quadrupole solution (top panels of Fig. 12) we see that the quadrupole term resolves the radial residuals in M1 and M2 ( $Y-X$  plane) and accounts for the residual  $B_Y$  and  $B_Z$  at M10-III near CA, but underestimates the northward field at M1 and M2. The regularized TS04-corrected solution (bottom panels of Fig. 12) yields lower north-south residuals at M10-III, M1, and M2 but gives larger residuals in the radial fields at M1, M2, and M10-I near CA and also in  $B_Y$  at M10-III. It appears that regularized higher-order solutions cannot simultaneously reduce the residuals in the radial and north-south directions in the equatorial plane, and this was confirmed to be a common characteristic of the inversions via a series of experiments using different choices of weights and misfit levels. The M10-I observations near CA cannot be explained by any of the models. There is also a suggestion of a horizontal component,  $B_Y$  in MBF coordinates, in M10-III observations over the pole that cannot be fit with higher-order internal field terms.

That the residuals are not ordered by radial distance (cf. Fig. 9) suggests that their spatial distribution should be considered in a coordinate system appropriate to the external current systems. In Fig. 13 we plot the residuals for models 5 and 7, TS04-corrected quadrupole (top panels) and regularized (bottom panels), in the same format as Fig. 12 but in MSO rather than MBF coordinates. The left-hand panels show the view looking toward the Sun, and the right-hand panels show the view looking southward from above the north pole.

We first focus on the M10-III residuals in the  $X-Y$  plane. The M10-III residuals in the  $X-Y$  plane are sunward and are somewhat localized to the polar region. These polar-region sunward residuals are indicative of a tilt in the magnetic field such that the lines of force are pulled tailward in a localized region over the polar cap, consistent with magnetospheric convection (e.g., Slavin et al. 2009b) and equivalent to the linked Birkeland field-aligned and horizontal ionospheric current system at Earth (e.g., Cowley 2000; Richmond and Thayer 2000; Anderson et al. 2008a). The possibility of such a system at Mercury has been proposed and is remarkable given that there is no ionosphere to carry the current as readily as at Earth (Glassmeier 1997; Slavin et al. 1997; Ip and Kopp 2004).

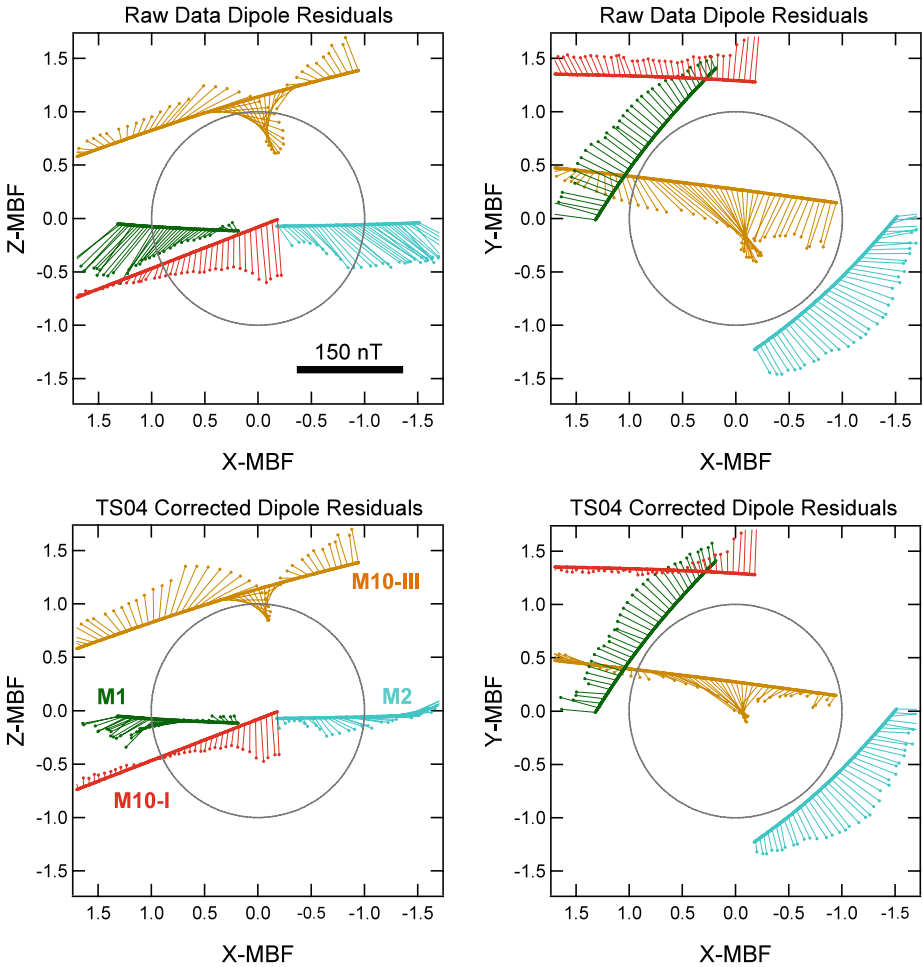


**Fig. 11** Overview of Mariner 10 and MESSENGER magnetic field data used for estimating the planetary internal magnetic field in the same format as Fig. 10 except that the length of an arrow corresponding to 150 nT is indicated in the top left panel. Data and trajectories are shown in MBF coordinates. The top panels show the residuals relative to a centered dipole fit to the observations (model 1 of Table 1), and the bottom panels show the residuals relative to a centered dipole fit to the observations that are first corrected for the TS04 external field (model 2 of Table 1)

Considering the M10-I, M1, and M2 residuals, it is evident that all of these data come from the nightside, so that these observations will be strongly influenced by the intensity and location of the cross-tail current system. The pronounced reversal in  $\delta B_X$  and  $\delta B_Z$  near CA for M10-I could reflect a sudden intensification of the cross-tail current. The data used here and selected for internal field modeling are those prior to the strong dynamic variations in the field that have been interpreted as a major substorm (Ogilvie et al. 1977; Christon 1987). The changes in  $\delta B_X$  and  $\delta B_Z$  could reflect the growth phase of the substorm, which at Earth is associated with both motion and intensification of the cross-tail current (cf. Parks 1991). The change observed by M10-I occurred over about 30 s, consistent with the magnetospheric convection timescale at Mercury (Christon 1987; Slavin et al. 2009b).

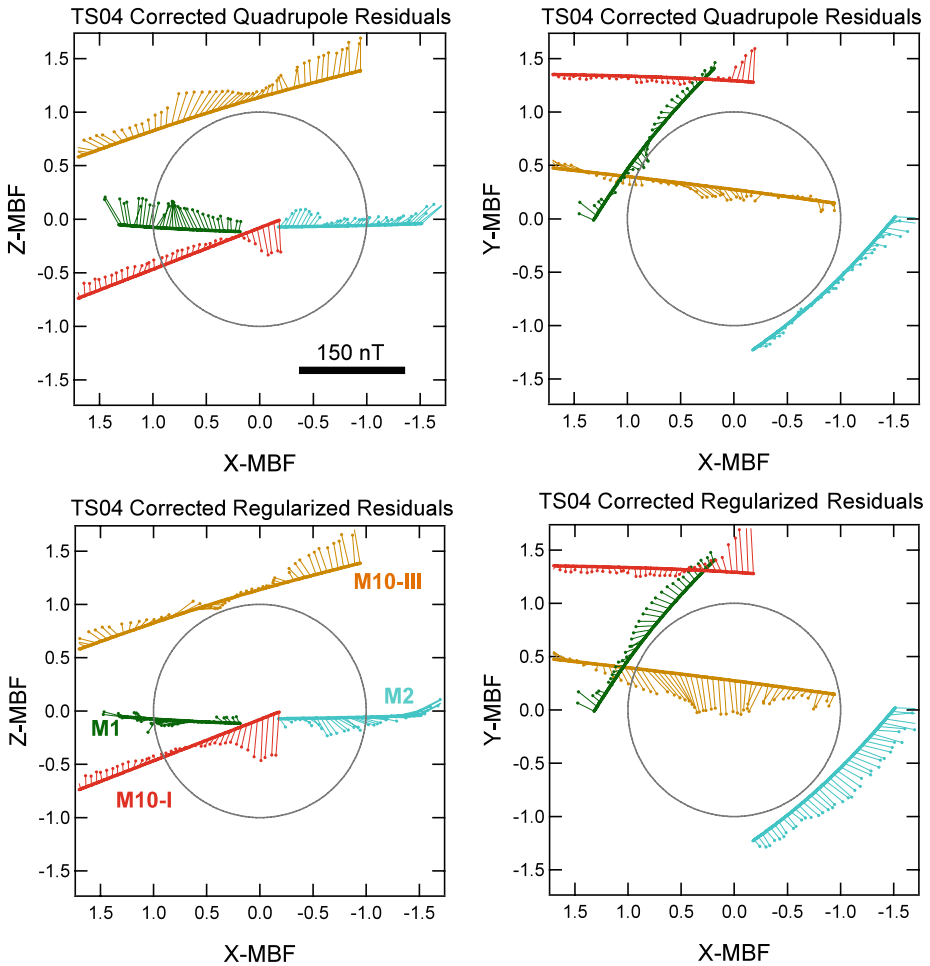


**Fig. 12** Overview of Mariner 10 and MESSENGER magnetic field data used for estimating the planetary internal magnetic field in the same format as Fig. 11. The length of an arrow corresponding to 150 nT is indicated in the *top left panel*. Data and trajectories are shown in MBF coordinates. The *top panels* show the residuals relative to a quadrupole fit to the observations, equivalent to an offset dipole, and the *bottom panels* show the residuals relative to the regularized solution of Uno (2009). All solutions are fit to observations that are first corrected for the TS04 external field

The M1 and M2 observations also indicate variability in the tail current system. The  $\delta B_X$  residuals for M1 and M2 are systematically different, with  $\delta B_X$  consistently stronger for M2 than for M1. As noted above, during M1 the MESSENGER spacecraft passed initially into the cross-tail current sheet and then into the plasma sheet of the southern tail lobe, whereas for M2 the spacecraft entered directly into the southern tail lobe. From the  $Z$ – $Y$  plane view, however, we see that the trajectories are almost identical relative to the mid-plane of the tail, with both nearly in the  $Z = 0$  plane. Thus, the current sheet must have been displaced northward for both M1 and M2, and for M2 the current sheet either was farther northward or the plasma sheet and current sheet were thinner. In addition, the cross-tail current may have been stronger for M2 than for M1.

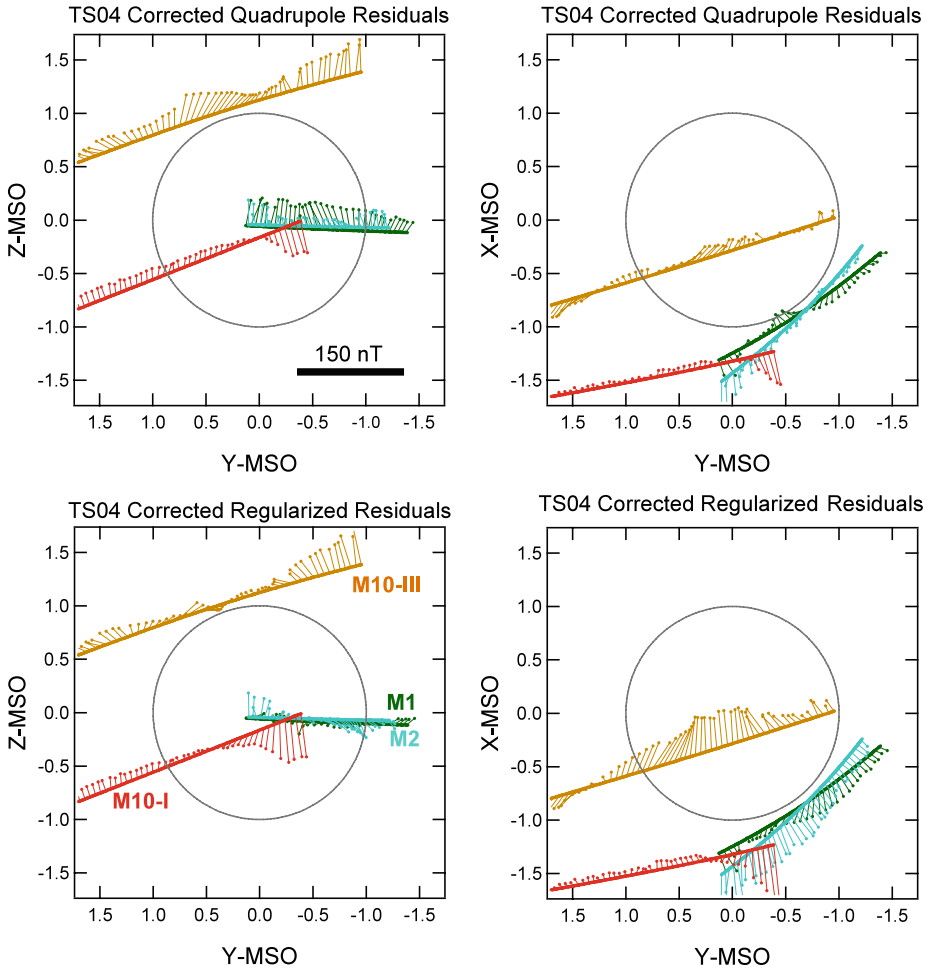


**Fig. 13** Overview of Mariner 10 and MESSENGER magnetic field data used for estimating the planetary internal magnetic field in the same format as Fig. 11 but with the data shown in MSO coordinates. *The top panels* show the residuals relative to a quadrupole fit to the observations, model 5 of Table 1, equivalent to an offset dipole, and *the bottom panels* show the residuals relative to the regularized solution of Uno (2009), model 7 of Table 1. All solutions are fit to observations that are first corrected for the TS04 external field

#### 5.4 Implications for Magnetospheric Currents

Since the structure and dynamics of external currents may be responsible for a major portion of the residuals, we now examine the data primarily to assess the magnetospheric current systems. In this we are guided by the hybrid simulations, which indicate an annulus of solar wind plasma within about  $0.5R_M$  altitude that extends around the nightside of the planet (Trávníček et al. 2007, 2009). This annulus has a radially inward pressure gradient, which implies an electric current  $\mathbf{J} = (\mathbf{B} \times \nabla P)/B^2$ , directed from dawn to dusk at midnight, where  $\mathbf{B}$  is the vector magnetic field and  $P$  is the scalar plasma pressure. The MESSENGER magnetic field and plasma observations presented above, Figs. 6 and 7, provide confirmation that solar wind plasmas are present close to the planet with densities sufficient to signifi-

cantly perturb the magnetic field. It is possible then, that departures from dipole signatures, particularly in the equatorial plane, may be due primarily to local magnetospheric currents rather than higher-order structure in the internal field. Thus, we now adopt the simplest possible interpretation for the internal field and assess what the remaining signatures imply if considered as due to external and local currents only.

Consider those magnetic sources in the Mercury system that can be identified with greatest confidence. Obviously, the planet possesses at least a dipolar magnetic field and therefore also magnetopause and magnetotail current systems. The higher-order inversions all yield a moment nearly aligned with the planetary rotation axis. Moreover, we are fairly sure that plasmas in the equatorial plane are present and influence the measurements made there. Under this conservative view, it may be that our best measure of the internal dipole is given by the M10-III flyby data. This inference is supported by the hybrid simulations, which do not indicate significant plasma densities over the polar region. We then corrected the M10-III data only for the magnetopause and distant tail currents using the TS04 model as implemented here, and fit a centered, axially aligned dipole to the corrected M10-III data only. This gives a moment of 266 nT- $R_M^3$ .

With this simplest possible model for the internal field we consider whether the remaining residuals can be understood in terms of external currents. The residuals of all of the data relative to the M10-III dipole fit are shown in Fig. 14. The top panels show the residuals without an external field correction, and the bottom panels show residuals after subtracting the TS04 external field. The residuals in the bottom panel should reflect uncorrected signatures of external currents relatively close to the planet under the assumption that the signatures of these currents dominate the residuals.

The equatorial passes all indicate radial and southward fields in the magnetotail close to the planet. For M1 and M2 toward the dawn terminator, the external field was directed somewhat more radially than tailward, suggesting that the cross-tail current may wrap around the planet in a manner analogous to the inter-relationship of the Earth's tail and ring-current systems (e.g., Tsyganenko 1995). The southward signatures in M10-I, M1, and M2 near the planet indicate that there is a dawn-to-dusk current just tailward of the spacecraft, perhaps as close as  $0.5R_M$  altitude. Hybrid simulations for M1 yielded a neutral sheet hosting such an azimuthal current north of the equator by almost  $0.5R_M$  at  $1R_M$  altitude, possibly in response to the  $X$ -component of the IMF (Trávníček et al. 2009). The IMF  $X$ -component was negative, anti-sunward for M2 and M1 (cf. Figs. 4 and 5), but positive for the inbound pass of M10-I, so it is not clear whether this mechanism can account for the tailward field near CA on the M10-I flyby.

We estimate the intensity of this near-tail azimuthal current as follows. If we assume that the M1 and M2 trajectories pass under the near-tail current, then the net change in magnetic field that it generates,  $\delta B$ , is twice the radial field observed, or about 100 nT, since the field switches sign across the current. The linear current sheet density is readily estimated as  $\delta B/\mu_0 = 80$  mA/m. If the current sheet is  $0.5R_M$  thick, consistent with the hybrid simulations, the current density would be  $\sim 0.1 \mu\text{A}/\text{m}^2$ , and if the sheet has a radial extent of  $\sim 1R_M$  the total current would be  $2 \times 10^5$  A. For comparison we show the current density distribution of the TS04 model for nominal solar wind IMF conditions at Mercury in Fig. 15. The plot shows the  $Y$  component of the current density in the dawn-dusk meridian. The dayside and tail magnetopause currents are most prominent, but the cross-tail current is clearly evident. In this model, the cross-tail current is appreciable only beyond  $X = -2R_M$ . The inferred current density for the near-tail current is well within the range of densities required to produce the TS04 tail configuration.

The residuals at M10-III are comparable to those near the nightside equator, so the axial dipole fit, even only to M10-III, is not sufficient to account for those data alone. The primary

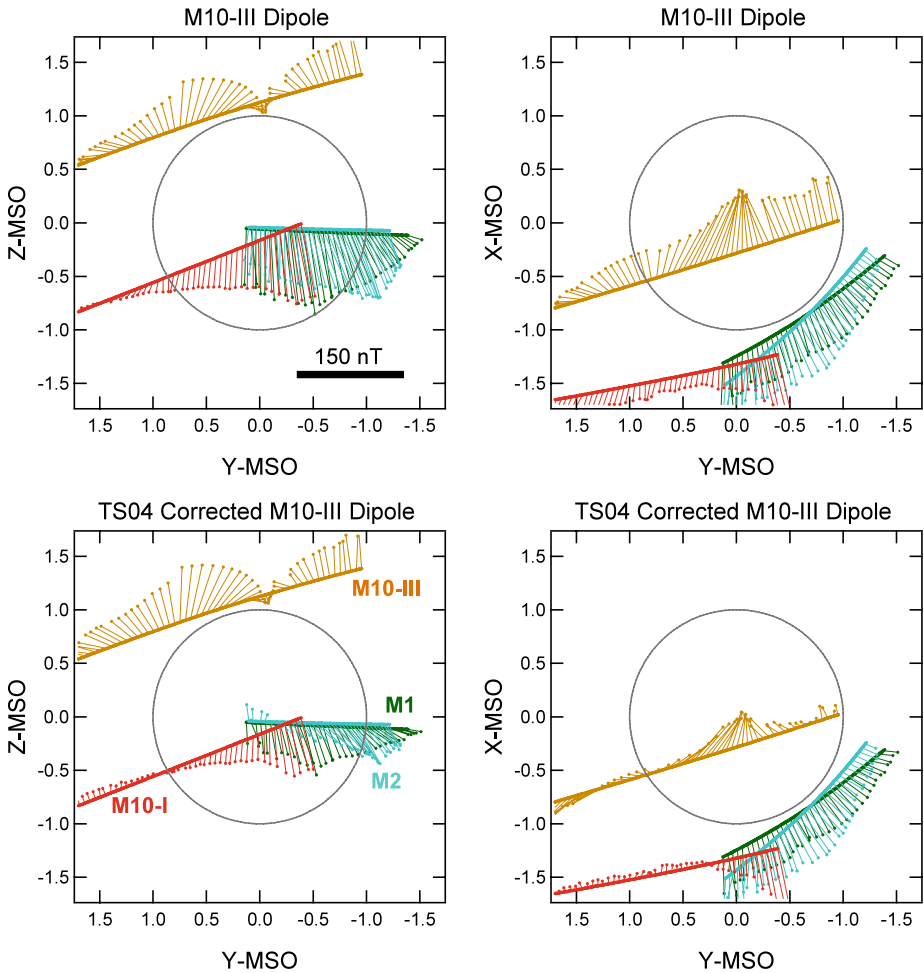


**Fig. 14** Overview of Mariner 10 and MESSENGER magnetic field data used for estimating the planetary internal magnetic field in the same format as Fig. 13. *The top panels show the residuals relative to a M10-III only, axially aligned dipole fit, and the bottom panels show the same residuals but also corrected for the TS04 external field*

departure is a predominant northward residual. To better understand the departure of the M10-III data from this simple dipole, we show in Fig. 16 the M10-III data corrected for the TS04 external field in Cartesian MSO coordinates together with the centered dipole fit and the residual from the fit. Comparing the observations with the fit shows that the residuals arise because the observed field is more confined to the region near the pole than would be the field from a centered axial dipole field. This is most evident in the  $Z$  component, where, although the peaks are the same, near  $-300$  nT for both the fit and the data, the observed field drops to zero more sharply on either side of the peak than does the dipole fit. The dipole field is similarly broader than the observed field in the  $X$  and  $Y$  components. We note that the distant field of the equatorial azimuthal current identified above cannot explain this discrepancy from the dipole because, although the equatorial current gives a field over the

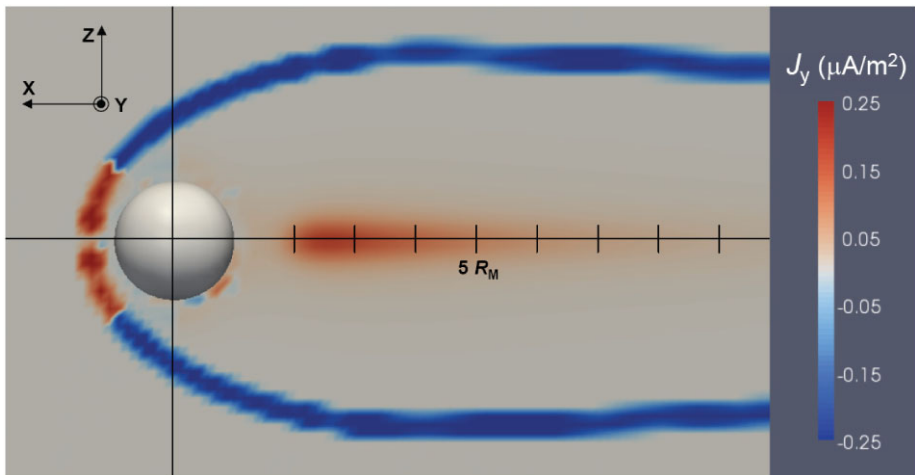


**Fig. 15** Current density distribution in the noon-midnight meridian plane calculated from the TS04 model scaled to Mercury. The model is evaluated for the same parameters as that shown in Fig. 1. The resolution of the magnetic field grid from which the currents are computed is  $0.15R_M$ . The current densities adjacent to the planet surface are spurious because of numerical errors in calculating  $J_y$  at the inner boundary of the magnetic field model. The high current densities on the magnetopause are thinner layers than resolved in this display, while the cross-tail current is spread over a significant range in  $Z$ . Even though the cross-tail current density is comparably low, the total cross-tail current matches the sum of the northern and southern lobe magnetopause currents

pole of the same sense as that from a dipole, it adds a field that is broader than that of the dipole.

The present observations do not provide sufficient information to establish whether this discrepancy is due to structure in the internal field or to the solar wind interaction. The lower-altitude M10-III residuals can be resolved by introducing higher-order terms in the planetary field (e.g., Fig. 8), but the persistence of residuals at higher altitudes (Fig. 9) suggest that this is not a complete explanation. Alternatively, we note that there are irregularities in the observed field, suggesting the possibility that plasma pressure effects are influencing these data as well. Although the polar region itself may be relatively devoid of plasmas, the boundary surface between the polar region and lower latitudes where the plasma is prominent may be a locus of strong pressure gradients and possibly currents. To distinguish between these possibilities we should know where the plasma boundaries are, whether the deviations from a dipolar field are ordered better in local time or by planetary longitude, and whether the field in the south is comparable to that in the north. Although these questions cannot be resolved with the single cut through the polar region by the M10-III flyby, observations from orbit should do so.

Lastly, we note that there is a relatively modest sunward perturbation in the field within about  $0.25R_M$  of the pole. This is indicated not only in Fig. 14 (bottom right) but also by both models 5 and 7 of Table 1, Fig. 13 (right-hand panels). This localized sunward perturbation could be consistent with a set of field-aligned currents, toward the planet in the morning and away from the planet in the evening (Slavin et al. 1997; Ip and Kopp 2004), analogous to the terrestrial Region-1 Birkeland currents (Iijima and Potemra 1976; Anderson et al. 2008a). Judging from Figs. 13 and 14, the perturbation may be as large as  $\sim 50$  nT, corresponding to a linear current density of  $\sim 40$  mA/m, which if integrated over  $\sim 0.5R_M$  (e.g., Ip and Kopp 2004) would give a total current of 50,000 A. This is within

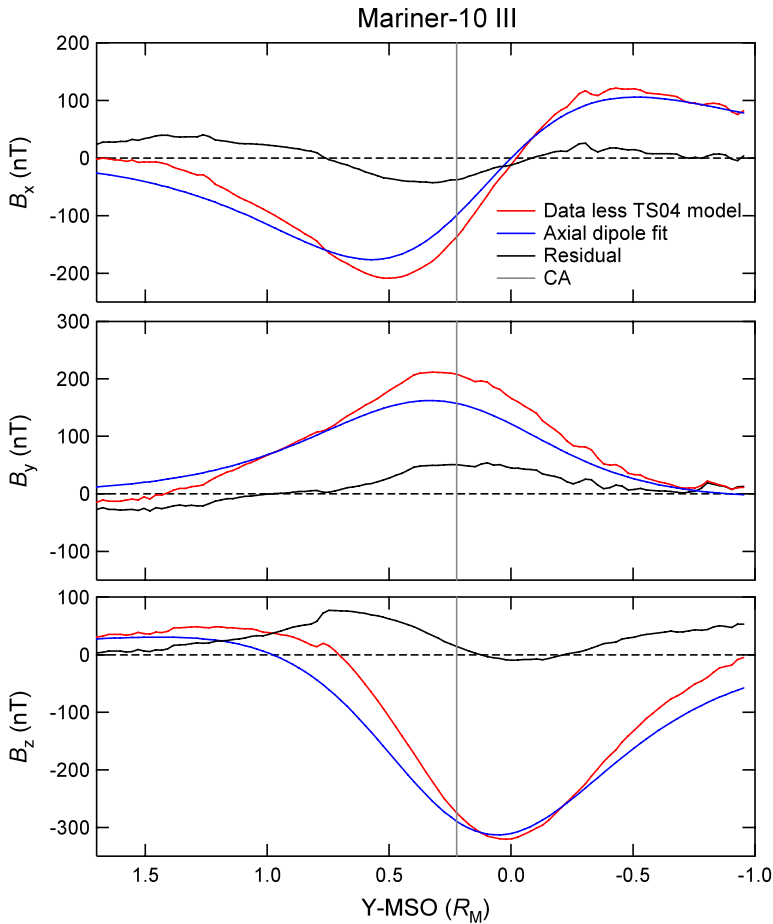


**Fig. 16** Mariner 10 III observations corrected for the TS04 external field (*red*) together with an axial dipole fit solely to these data (*blue*) and the residuals (*black*) plotted versus the spacecraft Y-MSO coordinate. The point of closest approach is indicated with the vertical grey line

the range estimated from simulations, though the simulation estimates are highly sensitive to the conductance assumed near the surface where the currents would close (Glassmeier 1997). Data from orbit should definitively establish whether Birkeland currents exist.

## 6 Assessment Looking Forward

Combining data from all of the flyby encounters with Mercury to date yields somewhat tighter constraints on the planetary dipole moment and clarifies the challenge of separating external contributions from higher-order terms in the internal field. The additional observations from the second MESSENGER flyby constrain the planetary moment to be nearly axially aligned and with a magnitude in the range 240 to 270 nT- $R_M^3$ . The new observations also confirm the presence of a cross-tail current close to the planet, which could account for the radial fields observed near the equator as well as the less strongly northward fields

there compared with expectations from a dipole fit to the M10-III data. The stronger dipole moment, near  $270 \text{ nT} \cdot R_M^3$ , therefore seems more likely. Nonetheless, the M10-III observations over the north pole cannot be understood solely in terms of a dipole field, implying either that the planetary pole field does possess higher-order structure or that the solar wind interaction influences the polar fields as well. Taken as a whole, then, the observations to date imply that magnetospheric currents close to the planet remain to be understood before definitive conclusions can be made about the structure of the internal field beyond the dipole. Nonetheless, higher-order inversion analysis of these data may prove useful to discriminate some mechanisms for the internal field generation, provided that the higher-order results are recognized as upper limits on the structure of the internal field. This analysis points to specific ways that observations from orbit together with physics-based simulations can be applied to resolve the ambiguities in our present understanding.

## 6.1 MESSENGER: First Orbital Observations

The MESSENGER spacecraft is on schedule for a final flyby of Mercury in September 2009 and orbit insertion in March 2011 (Solomon et al. 2007). The MESSENGER orbit at Mercury is designed to be highly elliptical, initially with periapsis at 200 km altitude and apoapsis at 15,000 km altitude,  $\sim 7.5 R_M$  planetocentric distance, an orbit inclination of  $\sim 80^\circ$ , and an orbit period of 12 hours (McAdams et al. 2007). The year-long baseline orbital mission will provide over 700 low-altitude passes over the northern polar region providing sampling spanning all local times and planetary longitudes. It will yield our first observations from the dayside magnetosphere of the planet. The orbit cuts through the equatorial region in a near ideal geometry to characterize the inferred equatorial currents and plasma enhancements. The orbit crosses the dayside magnetopause both at high and equatorial latitudes, providing excellent coverage to characterize the persistence of the boundary layer feature. Simulations predict large solar wind densities in the vicinity of the polar cusps (e.g., Trávníček et al. 2007), and the MESSENGER orbit should allow us to definitively establish this feature of the solar wind interaction as well. The MESSENGER observations from orbit will therefore lead to a number of advances key to understanding the internal field.

## 6.2 The BepiColombo Mission

The more ambitious two-spacecraft BepiColombo mission promises critical advances in definitively establishing the internal field of the planet (Balogh et al. 2007). The Mercury Planetary Orbiter (MPO) will orbit Mercury in a low-altitude polar orbit and provide the first low-altitude magnetic field observations over the southern polar region. The low-eccentricity polar orbit is well suited for the traditional spherical harmonic analyses of internal planetary magnetic fields for which the highly elliptical MESSENGER orbit is not ideal.

The profound influence of the solar wind interaction on the external field and the predominance of the external field contribution even at low altitudes imply that the simultaneous measurement of upstream conditions and the low-altitude magnetic field will be central in fully separating the internal and external field sources. This is an advance that the second BepiColombo spacecraft, the Mercury Magnetosphere Orbiter (MMO), will enable. The MMO spacecraft will provide sampling of the magnetosphere from an orbit different from that of MESSENGER and with a more complete plasma instrumentation package, thereby further advancing our understanding of the magnetosphere. But perhaps equally important for understanding the internal field, MMO will make simultaneous measurements of the solar wind and IMF to complement the low-altitude MPO observations, thus allowing dynamics observed at low altitudes to be related to variations in externally imposed conditions.

These two-point observations should allow not only higher fidelity in separating the external from internal field sources but also an ability to assess the role of fields produced by induced currents in the core (Glassmeier et al. 2007a, 2007b).

### 6.3 Modeling and Simulations

For the purpose of advancing our understanding of planetary magnetism, these planned observations of Mercury's magnetic field and magnetospheric environment should be matched by corresponding analyses to understand and predict the signatures of different processes generating the internal field (e.g., Zuber et al. 2007). It already appears that the prominent longitudinal structure of a remanent magnetic field (Aharonson et al. 2004) may not be consistent with the observations, though the longitudinal sampling is at present quite limited. Early orbital observations should resolve this question. If the field is dominated by the dipole term, as seems to be most probable, then we need to understand what signatures in the higher-order terms the different dynamo models should produce. Constraining the thickness of the fluid outer core is of great significance for this effort, since until we can constrain this dimension of the dynamo for the internal models, the magnetic field signatures alone may not prove decisive in distinguishing among competing models. The libration, gravity field, and topography of the planet are therefore essential to set limits on the internal structure, thereby helping to constrain the magnetic dynamo (Margot et al. 2007; Solomon et al. 2007; Zuber et al. 2007). In any case, the key to testing different models will be the accuracy of the higher-order terms, and so improved quantitative accuracy in the external field can be expected to impact our ability to discriminate among competing geophysical dynamo models to a degree that is disproportionate to the potentially modest improvement in external field knowledge.

The complexities of the magnetosphere of Mercury are unique in many respects (e.g., Baumjohann et al. 2006; Slavin et al. 2007), and it is to be expected that analogy from other magnetospheres will not apply, especially close to the planet where observations are most relevant to internal field estimation. Moreover, even the orbital sampling that the MESSENGER and BepiColombo missions are anticipated to provide will not yield exhaustive coverage of the magnetospheric volume, so that a quantitative understanding of the magnetosphere and hence the external field will likely require more than observations from orbit to fully resolve the external and internal fields. Physics-based simulations of the interaction will no doubt prove integral to guiding our quantitative specification of the natural system. One obvious approach in coupling the simulations with observations is to integrate the numerical simulations with the internal field inversion so that a physics-based external field is estimated together with the internal field terms (e.g., Jia et al. 2008). Formally we have already done this, because to specify the TS04 external model magnetopause and tail currents one must specify the internal field. We use an iterative process in which we take an initial estimate for the internal field, evaluate the TS04 model, subtract this from the observations, re-estimate the internal field and repeat these steps until the internal solution converges. This process yields an internal solution that typically converges to within one part in  $10^4$  after as few as four iterations. The same basic approach should be feasible with simulations.

Empirical external field models customized for Mercury will also play important roles for at least two reasons. First, it is likely to remain technically challenging to run a vast number of hybrid or even fluid simulations for the entire range of solar wind and IMF conditions imposed on the system. Thus, the physics-based simulation inversion analysis described above may remain applicable only to selected cases. Second, the physics-based simulations are sensitive to the boundary conditions and numerical diffusion responsible for mimicking reconnection processes. In particular, the conductivity distribution at the surface of the planet

is critical to obtaining currents and the distribution of electric fields and flows within the magnetosphere (Glassmeier 1997). To the extent that the assumed boundary conditions are at variance with the natural system, the currents and hence the external field of the simulations will be in error. Empirical models for the magnetospheric magnetic field analogous to those developed for Earth and other magnetized planets (Khurana 1997; Alexeev and Belenkaya 2005; Arridge et al. 2006; Alexeev et al. 2008) customized for Mercury will therefore remain an important tool. They offer the advantages that they are tied primarily to the observations, employ only specified known distributions of current, and can be evaluated rapidly for application to all of the observational data. Numerical simulations could also be used in tandem with the empirical models to inform the current system modules to be included.

The future is therefore very promising for progress on understanding the magnetic field of Mercury. Although many technical challenges remain, the stage appears to be set for a most exciting decade as the MESSENGER and BepiColombo missions return the first observations from orbit around the planet. These observations will in turn spur considerable work in modeling and numerical simulations to quantify our understanding of the processes generating the internal field as well as the dynamic and unique magnetosphere. New observations and powerful new modeling tools can be expected to tease out the secrets of the origin of the innermost planet's enigmatic magnetic field.

**Acknowledgements** We deeply mourn the loss of our colleague and MESSENGER Co-Investigator Mario Acuña during the preparation of this manuscript; his many contributions to the MESSENGER mission and the space science community live on. Assistance in visualizing magnetic field models from Alexander Ukhorskiy is gratefully acknowledged. The MESSENGER project is supported by the NASA Discovery Program under contracts NASW-00002 to the Carnegie Institution of Washington and NAS5-97271 to the Johns Hopkins University Applied Physics Laboratory. Support is also acknowledged from the NSERC Discovery Grant Program and the MESSENGER Participating Scientist Program (NNX07AR73G).

## References

- M.H. Acuña, J.E.P. Connerney, N.F. Ness, R.P. Lin, D. Mitchell, C.W. Carlson, J. McFadden, K.A. Anderson, H. Rème, C. Mazelle, D. Vignes, P. Wasilewski, P. Cloutier, *Science* **284**, 790 (1999)
- O. Aharonson, M.T. Zuber, S.C. Solomon, *Earth Planet. Sci. Lett.* **218**, 261 (2004)
- I.I. Alexeev, E. Belenkaya, *Ann. Geophys.* **23**, 809 (2005)
- I.I. Alexeev, E. Belenkaya, S.Yu. Bobrovnikov, J.A. Slavin, M. Sarantos, *J. Geophys. Res.* **113**, A12210 (2008). doi:[10.1029/2008JA013368](https://doi.org/10.1029/2008JA013368)
- B.J. Anderson, M.H. Acuña, D.A. Lohr, J. Scheifele, A. Raval, H. Korth, J.A. Slavin, *Space Sci. Rev.* **131**, 417 (2007)
- B.J. Anderson, H. Korth, C.L. Waters, D.L. Green, P. Stauning, *Ann. Geophys.* **26**, 671–687 (2008a)
- B.J. Anderson, M.H. Acuña, H. Korth, M.E. Purucker, C.L. Johnson, J.A. Slavin, S.C. Solomon, R.L. McNutt Jr., *Science* **321**, 82 (2008b)
- G.B. Andrews, T.H. Zurbuchen, B.H. Mauk, H. Malcom, L.A. Fisk, G. Gloeckler, G.C. Ho, J.S. Kelley, P.L. Koehn, T.W. LeFevre, S.S. Livi, R.A. Lundgren, J.M. Raines, *Space Sci. Rev.* **131**, 523 (2007)
- C.S. Arridge, N. Achilleos, M.K. Dogherty, K.K. Khurana, C.T. Russell, *J. Geophys. Res.* **111**, A11227 (2006). doi:[10.1029/2005JA011574](https://doi.org/10.1029/2005JA011574)
- G. Backus, *J. Geophys. Res.* **75**, 6339 (1970)
- A. Balogh, R. Grard, S.C. Solomon, R. Schulz, Y. Langevin, Y. Kasaba, M. Fujimoto, *Space Sci. Rev.* **132**, 611 (2007)
- W.A. Baumjohann, A. Matsuoka, K.-H. Glassmeier, C.T. Russell, T. Nagai, M. Hoshino, T. Nakagawa, A. Balogh, J.A. Slavin, R. Nakamura, W. Magnes, *Adv. Space Res.* **38**, 604 (2006)
- B. Chen, J. Li, S.A. Hauck II, *Geophys. Res. Lett.* **35**, L07201 (2008). doi:[10.1029/2008GL033311](https://doi.org/10.1029/2008GL033311)
- U.R. Christensen, *Nature* **444**, 1056 (2006)
- U.R. Christensen, J. Wicht, *Icarus* **196**, 16 (2008)
- S.P. Christon, *Icarus* **71**, 448 (1987)

- J.E.P. Connerney, N.F. Ness, in *Mercury*, ed. by F. Vilas, C.R. Chapman, M.S. Matthews (University of Arizona Press, Tucson, 1988), pp. 494–513
- S.W.H. Cowley, in *Magnetospheric Current Systems*, ed. by S. Ohtani, R. Fujii, M. Hesse, R.L. Lysak. Geophysical Monograph, vol. 118 (American Geophysical Union, Washington, 2000), pp. 91–106
- I.M. Engle, *Planet. Space Sci.* **45**, 127 (1997)
- G. Giampieri, A. Balogh, *Planet. Space Sci.* **49**, 1637 (2001)
- G. Giampieri, A. Balogh, *Planet. Space Sci.* **50**, 757 (2002)
- K.-H. Glassmeier, *Planet. Space Sci.* **45**, 119 (1997)
- K.-H. Glassmeier, in *Magnetospheric Current Systems*, ed. by S. Ohtani, R. Fujii, M. Hesse, R.L. Lysak. Geophysical Monograph, vol. 118 (American Geophysical Union, Washington, 2000), pp. 371–380
- K.-H. Glassmeier, J. Grosser, U. Auster, D. Constaninescu, Y. Narita, S. Stellmach, *Space Sci. Rev.* **132**, 511 (2007a)
- K.-H. Glassmeier, H.-U. Auster, U. Motschmann, *Geophys. Res. Lett.* **34**, L22201 (2007b). doi:[10.1029/2007GL031662](https://doi.org/10.1029/2007GL031662)
- J. Grosser, K.-H. Glassmeier, A. Stadelmann, *Planet. Space Sci.* **52**, 1251 (2004)
- S. Hauck, A. Dombard, R. Phillips, S.C. Solomon, *Earth Planet. Sci. Lett.* **222**, 713 (2004)
- M. Heimpel, J. Aurnou, F. Al-Shamali, N. Gomez Perez, *Earth Planet. Sci. Lett.* **236**, 542 (2005)
- T. Iijima, T.A. Potemra, *J. Geophys. Res.* **81**, 2165 (1976)
- W.-H. Ip, A. Kopp, *J. Geophys. Res.* **107**, 1348 (2002). doi:[10.1029/2001JA009171](https://doi.org/10.1029/2001JA009171)
- W.-H. Ip, A. Kopp, *Adv. Space Res.* **33**, 2172 (2004)
- Q. Jia, R.J. Walker, M.G. Kivelson, K.K. Khurana, J.A. Linker, *J. Geophys. Res.* **113**, A06212 (2008). doi:[10.1029/2007JA012748](https://doi.org/10.1029/2007JA012748)
- K.K. Khurana, *J. Geophys. Res.* **102**, 11295 (1997)
- H. Korth, B.J. Anderson, M.H. Acuña, J.A. Slavin, N.A. Tsyganenko, S.C. Solomon, R.L. McNutt Jr., *Planet. Space Sci.* **54**, 733 (2004)
- J.G. Luhmann, C.T. Russell, N.A. Tsyganenko, *J. Geophys. Res.* **103**, 9113 (1998)
- A.T.Y. Lui (ed.), *Magnetotail Physics* (The Johns Hopkins University Press, Baltimore, 1987), 433 pp
- J. Margot, S. Peale, R. Jurgens, M. Slade, I. Holin, *Science* **316**, 710 (2007)
- J.V. McAdams, R.W. Farquhar, A.H. Taylor, B.G. Williams, *Space Sci. Rev.* **131**, 219 (2007)
- W. Menke, *Geophysical Data Analysis: Discrete Inverse Theory* (Academic Press, San Diego, 1989), 289 pp
- N.F. Ness, K.W. Behannon, R.P. Lepping, Y.C. Whang, K.H. Schatten, *Science* **185**, 151 (1974)
- N.F. Ness, K.W. Behannon, R.P. Lepping, *J. Geophys. Res.* **80**, 2708 (1975)
- N.F. Ness, in *Solar System Plasma Physics*, vol. II, ed. by C.F. Kennel, L.J. Lanzerotti, E.N. Parker (North-Holland, New York, 1979), pp. 185–206
- K.W. Ogilvie, J.D. Scudder, V.M. Vasylunas, R.E. Hartle, G.L. Siscoe, *J. Geophys. Res.* **82**, 1807 (1977)
- G.K. Parks, *Physics of Space Plasmas, An Introduction* (Addison-Wesley, New York, 1991), 538 pp
- M.E. Purucker, T.J. Sabaka, S.C. Solomon, B.J. Anderson, H. Korth, M.T. Zuber, G.A. Neumann, *Earth. Planet. Sci. Lett.* (2009). doi:[10.1016/j.epsl.2008.12.017](https://doi.org/10.1016/j.epsl.2008.12.017)
- A.D. Richmond, J.P. Thayer, in *Magnetospheric Current Systems*, ed. by S. Ohtani, R. Fujii, M. Hesse, R.L. Lysak. Geophysical Monograph, vol. 118 (American Geophysical Union, Washington, 2000), pp. 131–146
- C.T. Russell, D.N. Baker, J.A. Slavin, in *Mercury*, ed. by F. Vilas, C.R. Chapman, M.S. Matthews (University of Arizona Press, Tucson, 1988), pp. 494–513
- G. Schubert, M. Ross, D. Stevenson, T. Spohn, in *Mercury*, ed. by F. Vilas, C.R. Chapman, M.S. Matthews (University of Arizona Press, Tucson, 1988), pp. 429–460
- D.G. Sibeck, R.E. Lopez, E.C. Roelof, *J. Geophys. Res.* **96**, 5489 (1991)
- J.-H. Shue, P. Song, C.T. Russell, J.T. Steinberg, J.K. Chao, G. Zastenker, O.L. Vaisberg, S. Kokubun, H.J. Singer, T.R. Detman, H. Kawano, *J. Geophys. Res.* **103**, 17691 (1998)
- J.A. Slavin, R.E. Holzer, *Phys. Earth Planet. Inter.* **20**, 231 (1979)
- J.A. Slavin, R.E. Holzer, *J. Geophys. Res.* **86**, 11401 (1981)
- J.A. Slavin, C.J. Owen, J.E.P. Connerney, S.P. Christon, *Planet. Space Sci.* **45**, 133 (1997)
- J.A. Slavin, S.M. Krimigis, M.H. Acuña, B.J. Anderson, D.N. Baker, P.L. Koehn, H. Korth, S.S. Livi, B.H. Mauk, S.C. Solomon, T.H. Zurbuchen, *Space Sci. Rev.* **131**, 133 (2007)
- J.A. Slavin, M.H. Acuña, B.J. Anderson, D.N. Baker, M. Benna, G. Gloeckler, R.E. Gold, G.C. Ho, R.M. Killen, H. Korth, S.M. Krimigis, R.L. McNutt Jr., L.R. Nittler, J.M. Raines, D. Schriver, S.C. Solomon, R.D. Starr, P. Trávníček, T.H. Zurbuchen, *Science* **321**, 85 (2008)
- J.A. Slavin, B.J. Anderson, T.H. Zurbuchen, D.N. Baker, S.M. Krimigis, M.H. Acuña, M. Benna, S.A. Boardson, G. Gloeckler, R.E. Gold, G.C. Ho, H. Korth, R.L. McNutt Jr., J.M. Raines, S. Menelaos, D. Schriver, S.C. Solomon, P. Trávníček, *Geophys. Res. Lett.* **36**, L02101 (2009a). doi:[10.1029/2008GL036158](https://doi.org/10.1029/2008GL036158)
- J.A. Slavin, M.H. Acuña, B.J. Anderson, D.N. Baker, M. Benna, S.A. Boardson, G. Gloeckler, R.E. Gold, G.C. Ho, H. Korth, S.M. Krimigis, R.L. McNutt Jr., J.M. Raines, M. Sarantos, D. Schriver, S.C. Solomon, P. Trávníček, T.H. Zurbuchen, *Science* **324**, 606 (2009b)

- S.C. Solomon, *Icarus* **28**, 509 (1976)
- S.C. Solomon, R.L. McNutt Jr., R.E. Gold, M.H. Acuña, D.N. Baker, W.V. Boynton, C.R. Chapman, A.F. Cheng, G. Gloeckler, J.W. Head III, S.M. Krimigis, W.E. McClintock, S.J. Peale, S.L. Murchie, R.J. Phillips, M.S. Robinson, J.A. Slavin, D.E. Smith, R.G. Strom, J.I. Trombka, M.T. Zuber, *Planet. Space Sci.* **49**, 1445–1465 (2001)
- S.C. Solomon, R.L. McNutt Jr., R.E. Gold, D.L. Domingue, *Space Sci. Rev.* **131**, 3 (2007)
- L.J. Srnka, *Phys. Earth Planet. Inter.* **11**, 184 (1976)
- S. Stanley, J. Bloxham, W. Hutchison, M. Zuber, *Earth Planet. Sci. Lett.* **234**, 27 (2005)
- S. Stanley, M. Zuber, J. Bloxham, *Geophys. Res. Lett.* **34** (2007). doi:[10.1029/2007GL030892](https://doi.org/10.1029/2007GL030892).
- A. Stephenson, *Earth Planet. Sci. Lett.* **28**, 454 (1976)
- D.J. Stevenson, *Rep. Prog. Phys.* **46**, 555 (1983)
- D.J. Stevenson, *Earth Planet. Sci. Lett.* **82**, 114–120 (1987)
- F. Takahashi, M. Matsushima, *Geophys. Res. Lett.* **33**, L10202 (2006). doi:[10.1029/2006GL02579](https://doi.org/10.1029/2006GL02579)
- P.M. Trávníček, P. Hellinger, D. Schriver, *Geophys. Res. Lett.* **34**, L05104 (2007). doi:[10.1029/2006GL028518](https://doi.org/10.1029/2006GL028518).
- P.M. Trávníček, P. Hellinger, D. Schriver, D. Herčík, J.A. Slavin, B.J. Anderson, *Geophys. Res. Lett.* **36**, L07104 (2009). doi:[10.1029/2008GL036630](https://doi.org/10.1029/2008GL036630).
- N.A. Tsyganenko, *J. Geophys. Res.* **100**, 5599 (1995)
- N.A. Tsyganenko, M.I. Sitnov, *J. Geophys. Res.* **110**, A03208 (2005). doi:[10.1029/2004JA010798](https://doi.org/10.1029/2004JA010798).
- H. Uno, MS Thesis, University of British Columbia, Vancouver, BC, Canada, 2009, 57 pp
- H. Uno, C.L. Johnson, B.J. Anderson, H. Korth, S.C. Solomon, *Earth. Planet. Sci. Lett.* (2009). doi:[10.1016/j.epsl.2009.02.032](https://doi.org/10.1016/j.epsl.2009.02.032)
- J. Wicht, M. Manda, F. Takahashi, U. Christensen, M. Matsushima, B. Langlais, *Space Sci. Rev.* **132**, 261 (2007)
- M.T. Zuber, O. Aharonson, J.M. Aurnou, A.F. Cheng, S.A. Hauck II, M.H. Heimpel, G.A. Neumann, S.J. Peale, R.J. Phillips, D.E. Smith, S.C. Solomon, S. Stanley, *Space Sci. Rev.* **131**, 105 (2007)
- T.H. Zurbuchen, J.M. Raines, G. Gloeckler, S.M. Krimigis, J.A. Slavin, P.L. Koehn, R.M. Killen, A.L. Sprague, R.L. McNutt Jr., S.C. Solomon, *Science* **321**, 90 (2008)